

ARMY RESEARCH LABORATORY



**Application of a Brittle Damage Model to
Normal Plate-on-Plate Impact**

by Martin N. Raftenberg

ARL-TR-3634

December 2005

NOTICES

Disclaimers

The findings in this report are not to be construed as an official Department of the Army position unless so designated by other authorized documents.

Citation of manufacturer's or trade names does not constitute an official endorsement or approval of the use thereof.

DESTRUCTION NOTICE—Destroy this report when it is no longer needed. Do not return it to the originator.

Army Research Laboratory

Aberdeen Proving Ground, MD 21005-5069

ARL-TR-3634

December 2005

Application of a Brittle Damage Model to Normal Plate-on-Plate Impact

Martin N. Raftenberg
Weapons and Materials Research Directorate, ARL

REPORT DOCUMENTATION PAGE

Form Approved
OMB No. 0704-0188

Public reporting burden for this collection of information is estimated to average 1 hour per response, including the time for reviewing instructions, searching existing data sources, gathering and maintaining the data needed, and completing and reviewing the collection information. Send comments regarding this burden estimate or any other aspect of this collection of information, including suggestions for reducing the burden, to Department of Defense, Washington Headquarters Services, Directorate for Information Operations and Reports (0704-0188), 1215 Jefferson Davis Highway, Suite 1204, Arlington, VA 22202-4302. Respondents should be aware that notwithstanding any other provision of law, no person shall be subject to any penalty for failing to comply with a collection of information if it does not display a currently valid OMB control number.

PLEASE DO NOT RETURN YOUR FORM TO THE ABOVE ADDRESS.

1. REPORT DATE (DD-MM-YYYY) December 2005		2. REPORT TYPE Final		3. DATES COVERED (From - To) October 2004 through September 2005	
4. TITLE AND SUBTITLE Application of a Brittle Damage Model to Normal Plate-on-Plate Impact				5a. CONTRACT NUMBER	
				5b. GRANT NUMBER	
				5c. PROGRAM ELEMENT NUMBER	
6. AUTHOR(S) Martin N. Raftenberg (ARL)				5d. PROJECT NUMBER 1L162618AH80	
				5e. TASK NUMBER	
				5f. WORK UNIT NUMBER	
7. PERFORMING ORGANIZATION NAME(S) AND ADDRESS(ES) U.S. Army Research Laboratory Weapons and Materials Research Directorate Aberdeen Proving Ground, MD 21005-5069				8. PERFORMING ORGANIZATION REPORT NUMBER ARL-TR-3634	
9. SPONSORING/MONITORING AGENCY NAME(S) AND ADDRESS(ES)				10. SPONSOR/MONITOR'S ACRONYM(S)	
				11. SPONSOR/MONITOR'S REPORT NUMBER(S)	
12. DISTRIBUTION/AVAILABILITY STATEMENT Approved for public release; distribution is unlimited.					
13. SUPPLEMENTARY NOTES					
14. ABSTRACT A brittle damage model presented by Grinfeld and Wright of the U.S. Army Research Laboratory was implemented in the LS-DYNA ¹ finite element code and applied to the simulation of normal plate-on-plate impact. The damage model introduces a state variable measure of damage that evolves in proportion to the elastic strain energy. The model degrades the elastic shear modulus in proportion to the state variable's current level. In a simulation of normal plate-on-plate impact, the model produced a gradient in elastic properties within the initially homogeneous target, and this gradient led to a partial reflection of the unloading wave. For a range of values for the material constants introduced by the damage model, the target's free-surface velocity showed a gradual increase over time following the arrival of the initial compressive shock. ¹ LS-DYNA, which is not an acronym, is a trademark of Livermore Software Technology Corp.					
15. SUBJECT TERMS brittle; damage model; failure waves; shock wave					
16. SECURITY CLASSIFICATION OF:			17. LIMITATION OF ABSTRACT SAR	18. NUMBER OF PAGES 65	19a. NAME OF RESPONSIBLE PERSON Martin N. Raftenberg
a. REPORT Unclassified	b. ABSTRACT Unclassified	c. THIS PAGE Unclassified			19b. TELEPHONE NUMBER (Include area code) 410-306-0949

Contents

List of Figures	v
List of Tables	vi
Acknowledgments	vii
1. Introduction	1
2. The Damage Model	3
2.1 Pre-damaged Material	3
2.2 Damage Evolution	3
2.3 Degradation Function	4
2.4 Calculation of Stresses	5
3. Implementation Into LS-DYNA	6
3.1 Generalization to Large Strain and Large Displacement	6
3.1.1 Pre-damaged Material	6
3.1.2 Damage Evolution and the Degradation Function	7
3.1.3 Calculation of Stresses	7
3.2 Implementation With the User Material Feature of LS-DYNA	8
3.3 Constant Stretch Rate Tension and Compression	8
3.3.1 Uniaxial Tension at a Constant Stretch Rate	8
3.3.2 Uniaxial Compression at a Constant Stretch Rate	13
4. Application to Normal Plate-on-Plate Impact	15
4.1 The Initial Value, Boundary Value Problem	15
4.2 Scaling the IVBVP	17
4.3 Dimensionless Parameter Π	18
4.4 Analytical Solution for the Case of No Damage ($\Pi = 0$)	18
4.5 Perturbation Procedure for the Case of Small Π	20
4.6 LS-DYNA Results for Various Values of Π	21
5. Conclusions	27

6. References	29
Appendix A. LS-DYNA Results for $\Pi = 0.1$	31
Appendix B. LS-DYNA Results for $\Pi = 0.3$	41
Appendix C. LS-DYNA Results for $\Pi = 0.126$	51
List of Symbols	58
Distribution List	60

List of Figures

Figure 1. The empirical evidence for failure waves: (a) VISAR signal on the rear surface of a K-19 glass target plate (reproduced from Kanel et al., 1992); (b) the hypothesized $x-t$ diagram for the target plate (reproduced from Brar and Bless, 1992).	2
Figure 2. Degradation function $\phi(D)$	5
Figure 3. An eight-node brick finite element subjected to uniaxial strain.	9
Figure 4. (a) The element in figure 3 is stretched at a constant positive (tensile) rate, and (b) D and S_{XX} evolve.	12
Figure 5. The solution to the problem in figure 3 evaluated with and without damage.	13
Figure 6. (a) The element in figure 3 is compressed at a constant negative stretch rate, and (b) D and S_{XX} evolve.	14
Figure 7. The boundary conditions imposed on the target in the uniaxial strain model of normal plate-on-plate impact (a) before and (b) after scaling.	16
Figure 8. The analytical $O(\Pi)$ solution evaluated for (a) $\Pi = 0.1$ and (b) $\Pi = 0.3$	22
Figure 9. FE mesh for the target plate: (a) entire thickness of the plate, (b) the $x = 0$ end.	23
Figure 10. Results for \hat{v}_x at $\hat{x} = 1$ (the free-surface normal velocity) as a function of \hat{t} and for various Π ($\phi_{\min} = 0.1$).	24
Figure 11. Results for D and ϕ as functions of \hat{x} at $\hat{t} = 1.5$ and for various Π ($\phi_{\min} = 0.1$).	25
Figure 12. $\hat{v}_x(\hat{x} = 1, \hat{t} = 2.000) - \hat{v}_x(\hat{x} = 1, \hat{t} = 1.125)$ as a function of Π ($\phi_{\min} = 0.1$).	27
Figure A-1. Contours of $\hat{\sigma}_{xx}$ across the target plate for $\Pi = 0.1$ and $\phi_{\min} = 0.1$.	
Figure A-2. $\hat{\sigma}_{xx}$ Contours in $\hat{x} - \hat{t}$ space for $\Pi = 0.1$ and $\hat{t} \in [0,1]$. ($\phi_{\min} = 0.1$).	32
Figure A-3. $\hat{\sigma}_{xx}$ Contours in $\hat{x} - \hat{t}$ space for $\Pi = 0.1$ and $\hat{t} \in [1,2]$. ($\phi_{\min} = 0.1$).	33
Figure A-4. Contours of D across the target plate for $\Pi = 0.1$ and $\phi_{\min} = 0.1$.	34
Figure A-5. Results for D as a function of \hat{x} for various \hat{t} and for $\Pi = 0.1$. ($\phi_{\min} = 0.1$).	35
Figure A-6. D Contours in $\hat{x} - \hat{t}$ space for $\Pi = 0.1$. ($\phi_{\min} = 0.1$).	36
Figure A-7. \hat{v}_x Contours in $\hat{x} - \hat{t}$ space for $\Pi = 0.1$ and $\hat{t} \in [0,1]$. ($\phi_{\min} = 0.1$).	37
Figure A-8. \hat{v}_x Contours in $\hat{x} - \hat{t}$ space for $\Pi = 0.1$ and $\hat{t} \in [1,2]$. ($\phi_{\min} = 0.1$).	38
Figure A-9. Enlargement of \hat{v}_x Contours in $\hat{x} - \hat{t}$ space for $\Pi = 0.1$ and $\hat{t} \in [1,2]$. ($\phi_{\min} = 0.1$).	39
Figure B-1. Contours of $\hat{\sigma}_{xx}$ across the target plate for $\Pi = 0.3$ and $\phi_{\min} = 0.1$.	
Figure B-2. $\hat{\sigma}_{xx}$ Contours in $\hat{x} - \hat{t}$ space for $\Pi = 0.3$ and $\hat{t} \in [0,1]$. ($\phi_{\min} = 0.1$).	42
Figure B-3. $\hat{\sigma}_{xx}$ Contours in $\hat{x} - \hat{t}$ space for $\Pi = 0.3$ and $\hat{t} \in [1,2]$. ($\phi_{\min} = 0.1$).	43
Figure B-4. Contours of D across the target plate for $\Pi = 0.3$ and $\phi_{\min} = 0.1$.	44

Figure B-5. Results for D as a function of \hat{x} for various \hat{t} and for $\Pi = 0.3$. ($\phi_{\min} = 0.1$).....	45
Figure B-6. D Contours in $\hat{x}-\hat{t}$ space for $\Pi = 0.3$. ($\phi_{\min} = 0.1$).	46
Figure B-7. \hat{v}_x Contours in $\hat{x}-\hat{t}$ space for $\Pi = 0.3$ and $\hat{t} \in [0,1]$. ($\phi_{\min} = 0.1$).....	47
Figure B-8. \hat{v}_x Contours in $\hat{x}-\hat{t}$ space for $\Pi = 0.3$ and $\hat{t} \in [1,2]$. ($\phi_{\min} = 0.1$).....	48
Figure B-9. Enlargement of \hat{v}_x Contours in $\hat{x}-\hat{t}$ space for $\Pi = 0.3$ and $\hat{t} \in [1,2]$. ($\phi_{\min} = 0.1$).....	49
Figure C-1. $\hat{\sigma}_{xx}$ Contours in $\hat{x}-\hat{t}$ space for $\Pi = 0.126$ and $\hat{t} \in [0,1]$. ($\phi_{\min} = 0.1$).....	51
Figure C-2. $\hat{\sigma}_{xx}$ Contours in $\hat{x}-\hat{t}$ space for $\Pi = 0.126$ and $\hat{t} \in [1,2]$. ($\phi_{\min} = 0.1$).....	52
Figure C-3. Results for D as a function of \hat{x} for various \hat{t} and for $\Pi = 0.126$. ($\phi_{\min} = 0.1$). ...	53
Figure C-4. D Contours in $\hat{x}-\hat{t}$ space for $\Pi = 0.126$. ($\phi_{\min} = 0.1$).....	54
Figure C-5. \hat{v}_x Contours in $\hat{x}-\hat{t}$ space for $\Pi = 0.126$ and $\hat{t} \in [0,1]$. ($\phi_{\min} = 0.1$).	55
Figure C-6. \hat{v}_x Contours in $\hat{x}-\hat{t}$ space for $\Pi = 0.126$ and $\hat{t} \in [1,2]$. ($\phi_{\min} = 0.1$).	56
Figure C-7. Enlargement of \hat{v}_x Contours in $\hat{x}-\hat{t}$ space for $\Pi = 0.126$ and $\hat{t} \in [1,2]$. ($\phi_{\min} = 0.1$).....	57

List of Tables

Table 1. Parameter values used in figure 4.....	13
Table 2. The scaled free-surface velocity, \hat{v}_x at $\hat{x} = 1$, for $\hat{t} = 1.125$, $\hat{t} = 2.000$, and the difference between the two for various Π ($\phi_{\min} = 0.1$).....	24

Acknowledgments

The author thanks Dr. Michael A. Grinfeld and Dr. Michael J. Scheidler, both of the U.S. Army Research Laboratory, for very helpful discussions of aspects of the damage model.

INTENTIONALLY LEFT BLANK

1. Introduction

Kanel et al. (1992) shock loaded K-19 glass in a normal plate-on-plate impact test, and the VISAR (velocity interferometer system for any reflector) measurement of normal velocity at the free surface contained a second plateau that they interpreted as evidence of a failure wave (figure 1a). Impact by the flyer plate introduces a compressive shock into the target plate. This compressive shock traverses the target plate and reaches the free surface, there producing an unloading wave that travels back toward the impacted surface. The hypothesis of Kanel et al. was that in K-19 glass, before reaching the impacted surface, the unloading wave encounters a slower moving failure front (figure 1b). The abrupt change in shock impedance at the failure front causes a partial reflection of the unloading wave. The reflected wave, upon reaching the free surface, produces a second plateau in the velocity signal.

To produce this hypothesized phenomenon in a simulation, a damage model should contain two features. First, the damage evolution equation should introduce one or more time scales, thereby allowing the damage front to lag the initial compressive shock. Second, the shock impedance should be substantially altered from its pre-damaged level.

A particular damage model that contains these features was presented, initially in an unpublished conference paper by Grinfeld and Wright (unpublished), and subsequently in the published conference paper Grinfeld, Schoenfeld, and Wright (in press). This model degrades the stiffness of an isotropic linearly elastic material. The model introduces a state variable that is a measure of damage. This state variable is initialized to zero and then monotonically grows according to an evolution equation that is based on elastic strain energy and introduces a single time scale. The damage model also consists of a degradation function, a function of the damage state variable, which is applied multiplicatively to the material's shear modulus. The damage model of Grinfeld and Wright is described in more detail in section 2.

The damage model of Grinfeld and Wright was installed into the LS-DYNA¹ finite element (FE) code via the user-material interface feature (Livermore Software Technology Corp., 2003). This implementation and the subsequent application of LS-DYNA to problems of constant stretch rate are described in section 3.

In section 4, the damage model is applied to simulations of normal plate-on-plate impact. First, an initial value, boundary value problem (IVBVP) is derived. Scaling of the IVBVP reveals the presence of a dimensionless group Π , which is a measure of the material's damage sensitivity. The LS-DYNA implementation was used to obtain solutions corresponding to a range of Π values. For certain Π values, the results for the target's free-surface velocity showed a gradual increase over time following the initial arrival of the compressive shock. For other Π values, the

¹LS-DYNA, which is not an acronym, is a trademark of Livermore Software Technology Corp.

free-surface velocity gradually decreased over time following the initial arrival of the compressive shock. These observations are summarized, and suggested modifications of the model are presented in section 5.

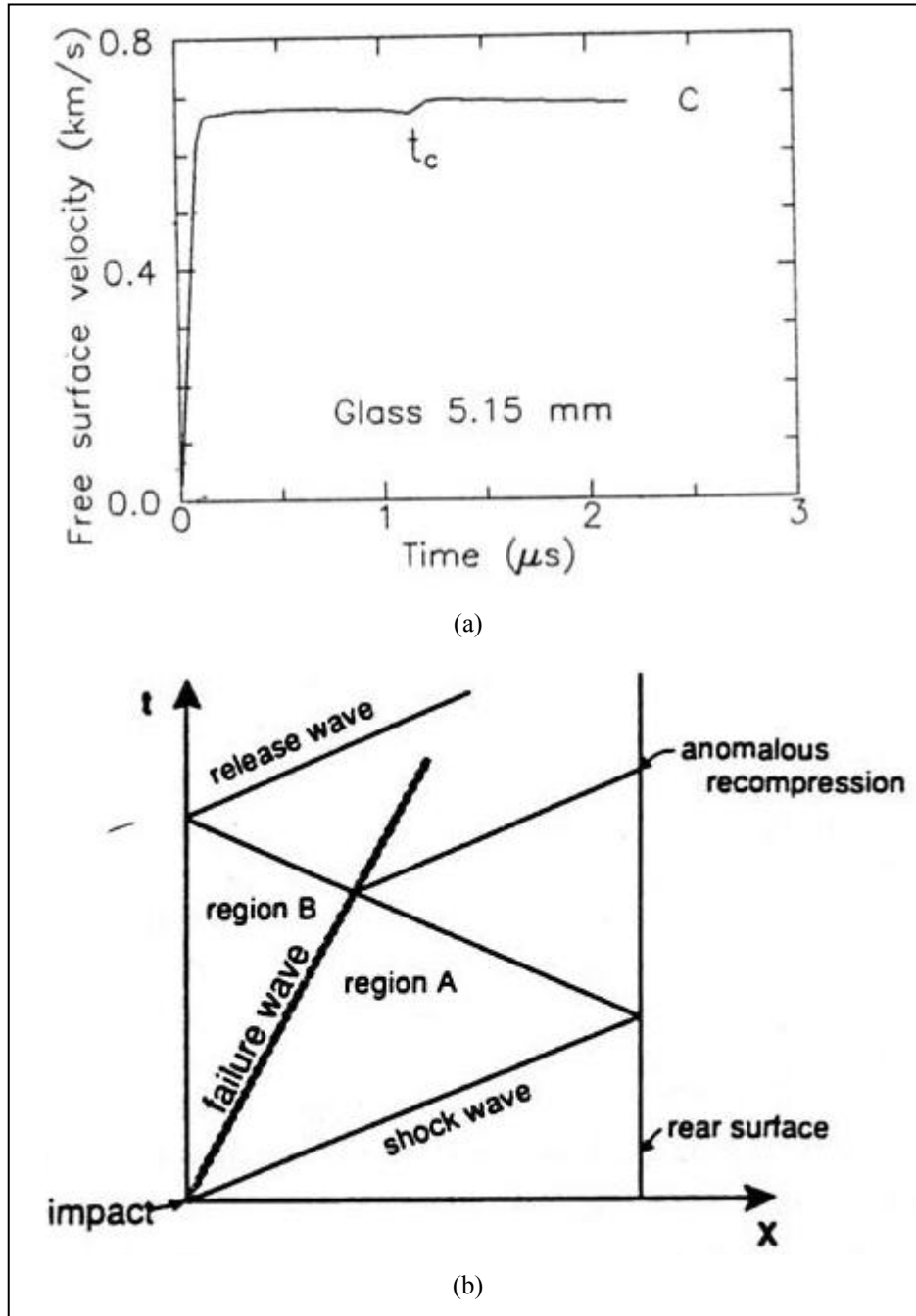


Figure 1. The empirical evidence for failure waves: (a) VISAR signal on the rear surface of a K-19 glass target plate (reproduced from Kanel et al., 1992); (b) the hypothesized $x-t$ diagram for the target plate (reproduced from Brar and Bless, 1992).

2. The Damage Model

The model for damage in brittle materials was developed by Grinfeld and Wright and presented in Grinfeld and Wright (unpublished) and Grinfeld et al. (in press). The components of the model are described in this section.

2.1 Pre-damaged Material

The model is applied to a material that in its pre-damaged state is isotropic and linearly elastic. Such a pre-damaged material is characterized by an elastic shear modulus, μ , Poisson ratio, ν , and density, ρ . The material's strain energy per unit volume, W_0 , is related to the infinitesimal strain tensor, \mathbf{e} , by

$$W_0(\mathbf{e}) = \mu \left(\frac{\nu}{1-2\nu} e_{ii} e_{jj} + e_{ij} e_{ij} \right) \quad (1)$$

in which the summation convention on repeated indices applies. In Cartesian coordinates, the components of \mathbf{e} are related to those of the displacement vector \mathbf{u} and position vector \mathbf{x} by

$$e_{ij} = \frac{1}{2} \left(\frac{\partial u_i}{\partial x_j} + \frac{\partial u_j}{\partial x_i} \right) \quad (2)$$

The conditions of small displacement and small strain have been assumed. Components of the Cauchy stress tensor $\boldsymbol{\sigma}$ are related to W_0 by

$$\sigma_{ij} = \frac{\partial W_0}{\partial e_{ij}} \quad (3)$$

2.2 Damage Evolution

The model of Grinfeld and Wright introduces damage effects by means of an internal state variable D that is a function of position and time. This variable is initialized to zero throughout the material. Thereafter, D monotonically increases according to the evolution equation

$$\dot{D} = -C \frac{\partial \psi}{\partial D} \quad (4)$$

Here, ψ is the Helmholtz free energy per unit volume and C is a material constant with dimensions of time \times distance/mass.

2.3 Degradation Function

Degradation function $\phi(D)$ is used to decrease the material's stiffness as damage accrues. $\phi(D)$ relates the Helmholtz free energy density of the damaged material to the elastic strain energy density by

$$\psi(\mathbf{e}, D) = \phi(D) W_0(\mathbf{e}) \quad (5)$$

Grinfeld and Wright assumed ϕ to be linearly related to D according to

$$\phi(D) = 1 - (1 - \phi_{\min})D \quad (6)$$

where ϕ_{\min} is a second material constant introduced by the model (C in equation 4 was the first). Equation 6 is sketched in figure 2. This dimensionless constant ϕ_{\min} is used to specify the residual stiffness of fully damaged material; ϕ_{\min} satisfies the restriction

$$0 \leq \phi_{\min} \leq 1 \quad (7)$$

The lower limit corresponds to the case of zero residual stiffness and the upper limit to the case of no degradation of stiffness. The combination of equations 4, 5, and 6 yields

$$\dot{D} = (1 - \phi_{\min})C \cdot \mu \left(\frac{\nu}{1 - 2\nu} e_{ii} e_{jj} + e_{ij} e_{ij} \right) \quad (8)$$

Coleman and Gurtin (1967) applied the Clausius-Duhem Inequality (the statement that the rate of entropy production must be non-negative) to material models involving one or more internal state variables. For the special case of effectively isothermal conditions (negligible spatial gradients of temperature and time rates of change of temperature) and a single internal state variable D , the Clausius-Duhem Inequality requires that

$$\frac{\partial \psi}{\partial D} \dot{D} \leq 0 \quad (9)$$

Equations 4 and 9 lead to the requirement that

$$C \geq 0 \quad (10)$$

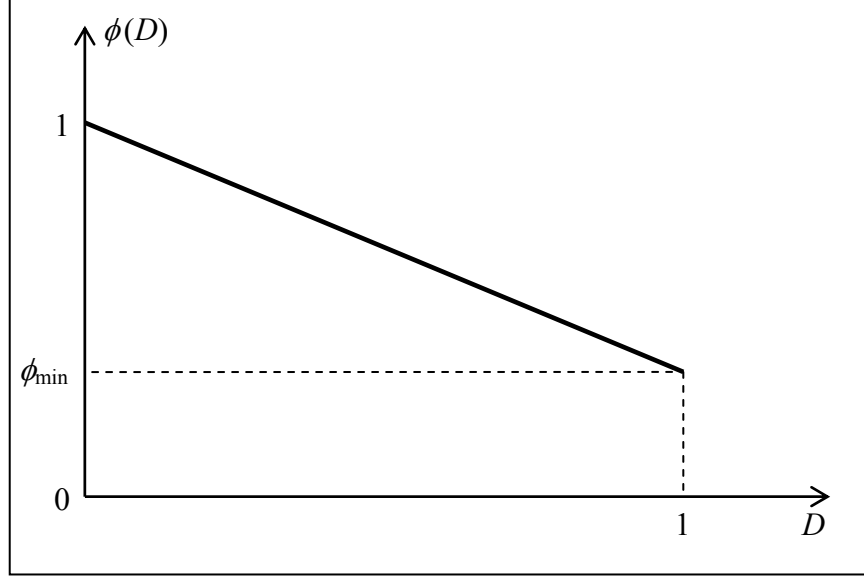


Figure 2. Degradation function $\phi(D)$.

2.4 Calculation of Stresses

Coleman and Gurtin (1967) also established a relationship between stress and the Helmholtz free energy that follows as a consequence of applying the Clausius-Duhem Inequality to a material model involving internal state variables. In our special case of a single internal state variable D and small deformations, Coleman and Gurtin showed equation 3 to be generalizable to

$$\sigma_{ij} = \frac{\partial \psi}{\partial e_{ij}} \quad (11)$$

From equation 5,

$$\sigma_{ij} = \phi(D) \frac{\partial W_0}{\partial e_{ij}} \quad (12)$$

The combination of equations 1 and 12 yields the stress-strain relation

$$\sigma_{ij} = 2\phi(D)\mu \left(\frac{\nu}{1-2\nu} e_{kk} \delta_{ij} + e_{ij} \right) \quad (13)$$

in which δ_{ij} is the Kronecker delta function. The components of the Cauchy stress tensor are then

$$\sigma_{xx} = \phi(D) \frac{2\mu}{1-2\nu} \left[(1-\nu)e_{xx} + \nu(e_{yy} + e_{zz}) \right] \quad (14a)$$

$$\sigma_{yy} = \phi(D) \frac{2\mu}{1-2\nu} \left[(1-\nu)e_{yy} + \nu(e_{xx} + e_{zz}) \right] \quad (14b)$$

$$\sigma_{zz} = \phi(D) \frac{2\mu}{1-2\nu} \left[(1-\nu)e_{zz} + \nu(e_{xx} + e_{yy}) \right] \quad (14c)$$

$$\sigma_{xy} = \phi(D) 2\mu e_{xy} \quad (14d)$$

$$\sigma_{yz} = \phi(D) 2\mu e_{yz} \quad (14e)$$

$$\sigma_{zx} = \phi(D) 2\mu e_{zx} \quad (14f)$$

This completes specification of the model presented by Grinfeld and Wright (unpublished).

3. Implementation Into LS-DYNA

3.1 Generalization to Large Strain and Large Displacement

Prior to implementation of the damage model into FE software, it was first generalized to apply to problems involving large displacements and large strains. (In a proper application to a brittle material, the model is unlikely to encounter large strains, but large displacements and rotations cannot be ruled out.) The relevant continuum mechanics concepts are explained further in Malvern (1969).

3.1.1 Pre-damaged Material

In the expression for the elastic strain energy density function, the infinitesimal strain tensor is replaced with the Green strain tensor \mathbf{E} , i.e.,

$$W_0(\mathbf{E}) = \mu \left(\frac{\nu}{1-2\nu} E_{ii} E_{jj} + E_{ij} E_{ij} \right) \quad (15)$$

where \mathbf{E} is defined in terms of the deformation gradient tensor \mathbf{F} and the identity tensor \mathbf{I} by

$$\mathbf{E} = \frac{1}{2} (\mathbf{F}^T \cdot \mathbf{F} - \mathbf{I}) \quad (16)$$

In Cartesian coordinates, equation 16 is expressed in terms of the displacement vector \mathbf{u} and the material coordinate vector \mathbf{X} by

$$E_{ij} = \frac{1}{2} \left(\frac{\partial u_i}{\partial X_j} + \frac{\partial u_j}{\partial X_i} + \frac{\partial u_k}{\partial X_i} \frac{\partial u_k}{\partial X_j} \right) \quad (17)$$

The second Piola-Kirchhoff stress \mathbf{S} is then computed from

$$S_{ij} = \frac{\partial W_0}{\partial E_{ij}} \quad (18)$$

and the Cauchy stress $\boldsymbol{\sigma}$ is computed from

$$\boldsymbol{\sigma} = \frac{\mathbf{F} \cdot \mathbf{S} \cdot \mathbf{F}^T}{\det \mathbf{F}} \quad (19)$$

3.1.2 Damage Evolution and the Degradation Function

Equations 4 and 6 still apply. Helmholtz free energy density is now a function of D and \mathbf{E} , i.e.,

$$\psi(\mathbf{E}, D) = \phi(D) W_0(\mathbf{E}) \quad (20)$$

and equation 8 is replaced with

$$\dot{D} = (1 - \phi_{\min}) C \cdot \mu \left(\frac{\nu}{1 - 2\nu} E_{ii} E_{jj} + E_{ij} E_{ij} \right) \quad (21)$$

3.1.3 Calculation of Stresses

In order to satisfy the property of frame indifference, it is convenient to work with the second Piola-Kirchhoff stress \mathbf{S} rather than directly with $\boldsymbol{\sigma}$. Equation 11 is replaced with

$$S_{ij} = \frac{\partial \psi}{\partial E_{ij}} \quad (22)$$

which, with equations 15 and 20, yields the stress-strain relation in terms of the second Piola-Kirchhoff stress and the Green strain.

$$S_{ij} = 2 \phi(D) \mu \left(\frac{\nu}{1 - 2\nu} E_{kk} \delta_{ij} + E_{ij} \right) \quad (23)$$

The six individual components of \mathbf{S} are

$$S_{xx} = \phi(D) \cdot \frac{2\mu}{1 - 2\nu} \left[(1 - \nu) E_{xx} + \nu (E_{yy} + E_{zz}) \right] \quad (24a)$$

$$S_{yy} = \phi(D) \cdot \frac{2\mu}{1 - 2\nu} \left[(1 - \nu) E_{yy} + \nu (E_{xx} + E_{zz}) \right] \quad (24b)$$

$$S_{zz} = \phi(D) \cdot \frac{2\mu}{1 - 2\nu} \left[(1 - \nu) E_{zz} + \nu (E_{xx} + E_{yy}) \right] \quad (24c)$$

$$S_{xy} = \phi(D) \cdot 2\mu E_{xy} \quad (24d)$$

$$S_{yz} = \phi(D) \cdot 2\mu E_{yz} \quad (24e)$$

$$S_{zx} = \phi(D) \cdot 2\mu E_{zx} \quad (24f)$$

As with the pre-damaged material, equation 19 again determines the Cauchy stress tensor σ .

3.2 Implementation With the User Material Feature of LS-DYNA

LS-DYNA offers a user material interface whereby a user-provided FORTRAN subroutine can be linked to the remainder of the code. The user sets up an array of material constants (in this case ρ , μ , ν , C , and ϕ_{\min}) and identifies one or more “history variables” (in this case D). The subroutine is called for every element at every time step. The code passes to the subroutine the material constants, \mathbf{F} for the current time step, and D from the previous time step, and the subroutine returns the Cauchy stress tensor σ .

The flow of the calculations is as follows. Equation 16 is used to compute \mathbf{E} . Equation 21 is integrated to update D as

$$D^{(e)}(t) = D^{(e)}(t - \Delta t) + (1 - \phi_{\min}) C \mu \left(\frac{\nu}{1 - 2\nu} E_{ii}^{(e)} E_{jj}^{(e)} + E_{ij}^{(e)} E_{ij}^{(e)} \right) \Delta t \quad (25)$$

The “(e)” superscript indicates application to a particular finite element. Equation 6 updates ϕ , equations (24a–f) update \mathbf{S} , and equation 19 updates σ .

3.3 Constant Stretch Rate Tension and Compression

In order to study features of the damage model prior to its application to normal plate-on-plate impact, the model was first applied to problems involving a prescribed constant stretch rate.

3.3.1 Uniaxial Tension at a Constant Stretch Rate

Figure 3 shows a single eight-node hexagonal “brick” element. Note the material and spatial coordinate systems defined in the figure. The “shape function” of this eight-node element restricts its internal velocity field to the following quadratic form in x , y , and z :

$$v_x(x, y, z, t) = a_x(t) + b_x(t)x + c_x(t)y + d_x(t)z + e_x(t)xy + f_x(t)xz + g_x(t)yz \quad (26a)$$

$$v_y(x, y, z, t) = a_y(t) + b_y(t)x + c_y(t)y + d_y(t)z + e_y(t)xy + f_y(t)xz + g_y(t)yz \quad (26b)$$

$$v_z(x, y, z, t) = a_z(t) + b_z(t)x + c_z(t)y + d_z(t)z + e_z(t)xy + f_z(t)xz + g_z(t)yz \quad (26c)$$

in which v_x , v_y , and v_z are the three components of velocity. The coefficients $a_x(t), b_x(t), \dots, g_z(t)$ are functions only of time.

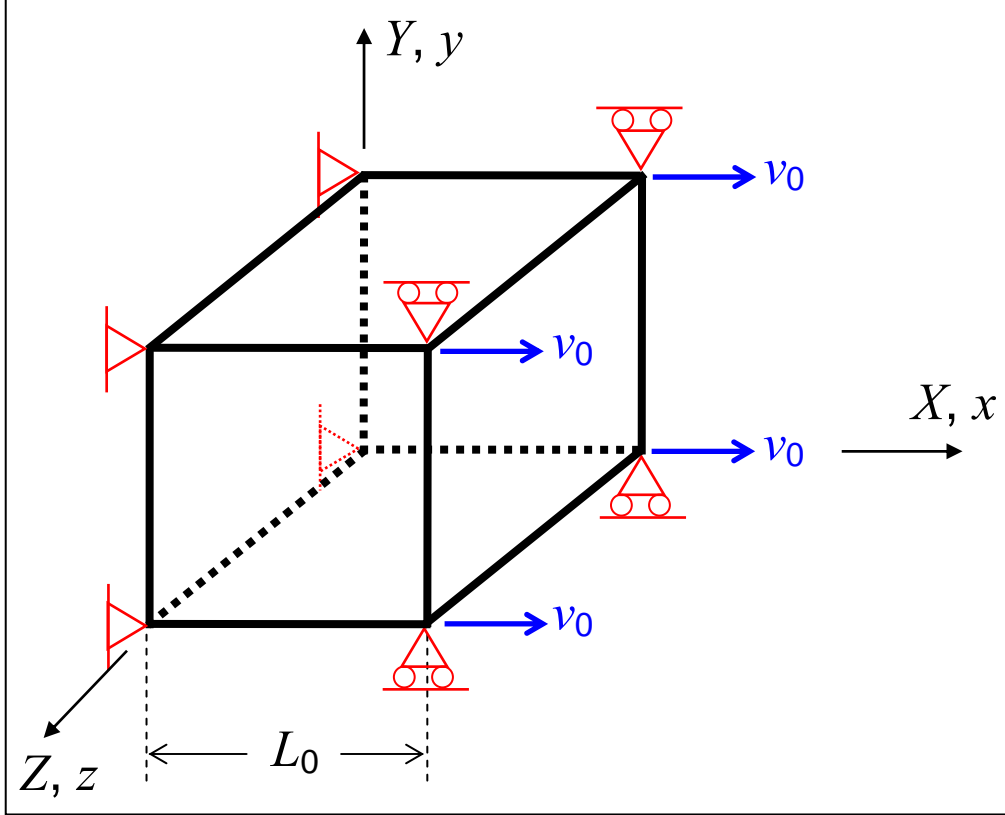


Figure 3. An eight-node brick finite element subjected to uniaxial strain.

At time $t = 0$, the element in figure 3 is a cube with edge length L_0 . Thereafter, a time-independent x -velocity v_0 is imposed on the four nodes of the face $X = L_0$. At these same four nodes, the y - and z -velocities are held at zero. At the four nodes of the opposite face, defined by $X = 0$, all three velocity components are held at zero. The boundary conditions of the problem are therefore

$$v_x(L_0, Y, Z, t) = v_0 t \quad (27a)$$

$$v_x(0, Y, Z, t) = v_y(0, Y, Z, t) = v_z(0, Y, Z, t) = v_y(L_0, Y, Z, t) = v_z(L_0, Y, Z, t) = 0 \quad (27b)$$

$$\forall Y, Z \in [0, L_0]$$

Once conditions 27a and 27b are imposed on the shape functions of equations 26a–c, we find that motion throughout the element is described by the mapping

$$x(X, t) = X + \frac{v_0 t}{L_0} X = \left(1 + \frac{v_0 t}{L_0}\right) X \quad (28a)$$

$$y = Y \quad (28b)$$

$$z = Z \quad (28c)$$

Equations 28a-c are exact, regardless of how fast one pulls the element. There are no inertia effects in this single-element problem, which makes it a useful vehicle for isolating effects of the constitutive model.

Thus, the deformation gradient tensor is

$$\mathbf{F}(\mathbf{t}) = \frac{\partial \mathbf{x}}{\partial \mathbf{X}} = \begin{bmatrix} 1 + \frac{v_0 t}{L_0} & 0 & 0 \\ 0 & 1 & 0 \\ 0 & 0 & 1 \end{bmatrix} \quad (29)$$

and the Green strain tensor is

$$\mathbf{E}(\mathbf{t}) = \frac{1}{2}(\mathbf{F}^T \cdot \mathbf{F} - \mathbf{I}) = \begin{bmatrix} \frac{v_0 t}{L_0} \left(1 + \frac{v_0 t}{2L_0}\right) & 0 & 0 \\ 0 & 0 & 0 \\ 0 & 0 & 0 \end{bmatrix} \quad (30)$$

Note that the strain is spatially constant throughout the element. If the strain is small, then there is little difference between strain and stretch, i.e.,

$$E_{xx}(t) = \frac{v_0 t}{L_0} \left(1 + \frac{v_0 t}{2L_0}\right) \cong \frac{v_0 t}{L_0} \quad (31)$$

and our constant stretch rate corresponds approximately to a constant strain rate; call it \dot{E} .

$$\dot{E}_{xx} \cong \frac{v_0}{L_0} \equiv \dot{E} \quad (32)$$

The elastic strain energy density throughout the element is then

$$W_0(t) = \mu \left(\frac{\nu}{1-2\nu} E_{ii} E_{jj} + E_{ij} E_{ij} \right) \cong \frac{(1-\nu)\mu}{1-2\nu} (E_{xx}(t))^2 = \frac{(1-\nu)\mu}{1-2\nu} (\dot{E}t)^2 \quad (33)$$

The damage evolution equation becomes

$$\frac{dD}{dt} = (1 - \phi_{\min}) C \cdot W_0(t) = (1 - \phi_{\min}) C \cdot \frac{(1-\nu)\mu}{1-2\nu} (\dot{E}t)^2 \quad (34)$$

The solution, assuming no initial damage at time zero, is the cubic in time

$$D(t) = (1 - \phi_{\min}) C \cdot \frac{(1-\nu)\mu}{3(1-2\nu)} \cdot \dot{E}^2 t^3 \quad (35)$$

However, this solution must be modified to take account of the upper bound of 1, reached at some time t^* determined from

$$D(t^*) = (1 - \phi_{\min})C \cdot \frac{(1 - \nu)\mu}{3(1 - 2\nu)} \cdot \dot{E}^2 (t^*)^3 = 1$$

to be

$$t^* = \left[\frac{1}{(1 - \phi_{\min})C} \cdot \frac{3(1 - 2\nu)}{(1 - \nu)\mu} \right]^{1/3} \cdot \dot{E}^{-2/3} \quad (36)$$

This provides a time scale associated with damage evolution. The time scale decreases with increasing strain rate. The two-part solution for D is then

$$D(t) = \begin{cases} \left(\frac{t}{t^*} \right)^3 & ; \quad 0 \leq t < t^* \\ 1 & ; \quad t \geq t^* \end{cases} \quad (37)$$

The degradation function is

$$\phi(t) = 1 - (1 - \phi_{\min})D = \begin{cases} 1 - (1 - \phi_{\min}) \left(\frac{t}{t^*} \right)^3 & ; \quad 0 \leq t < t^* \\ \phi_{\min} & ; \quad t \geq t^* \end{cases} \quad (38)$$

In order to calculate stress, we return to equation 33.

$$W_0 = \frac{(1 - \nu)\mu}{1 - 2\nu} \cdot E_{XX}^2 \quad (39)$$

Then

$$S_{XX} = \phi(D) \frac{\partial W_0}{\partial E_{XX}} = \phi(D) \cdot \frac{2(1 - \nu)\mu}{1 - 2\nu} \cdot E_{XX}$$

From equation 31,

$$S_{XX}(t) = \phi(t) \cdot \frac{2(1 - \nu)\mu}{1 - 2\nu} \cdot \dot{E} t$$

so that

$$S_{XX}(t) = \frac{2(1 - \nu)\mu}{1 - 2\nu} \cdot \dot{E} t \cdot \begin{cases} \left[1 - (1 - \phi_{\min}) \left(\frac{t}{t^*} \right)^3 \right] & ; \quad 0 \leq t < t^* \\ \phi_{\min} & ; \quad t \geq t^* \end{cases} \quad (40)$$

In figure 4, equations 36, 37, and 40 have been evaluated with the use of the material properties in table 1. In addition, the same problem was modeled with LS-DYNA, and the numerical results were virtually indistinguishable from the analytical results plotted in figure 4.

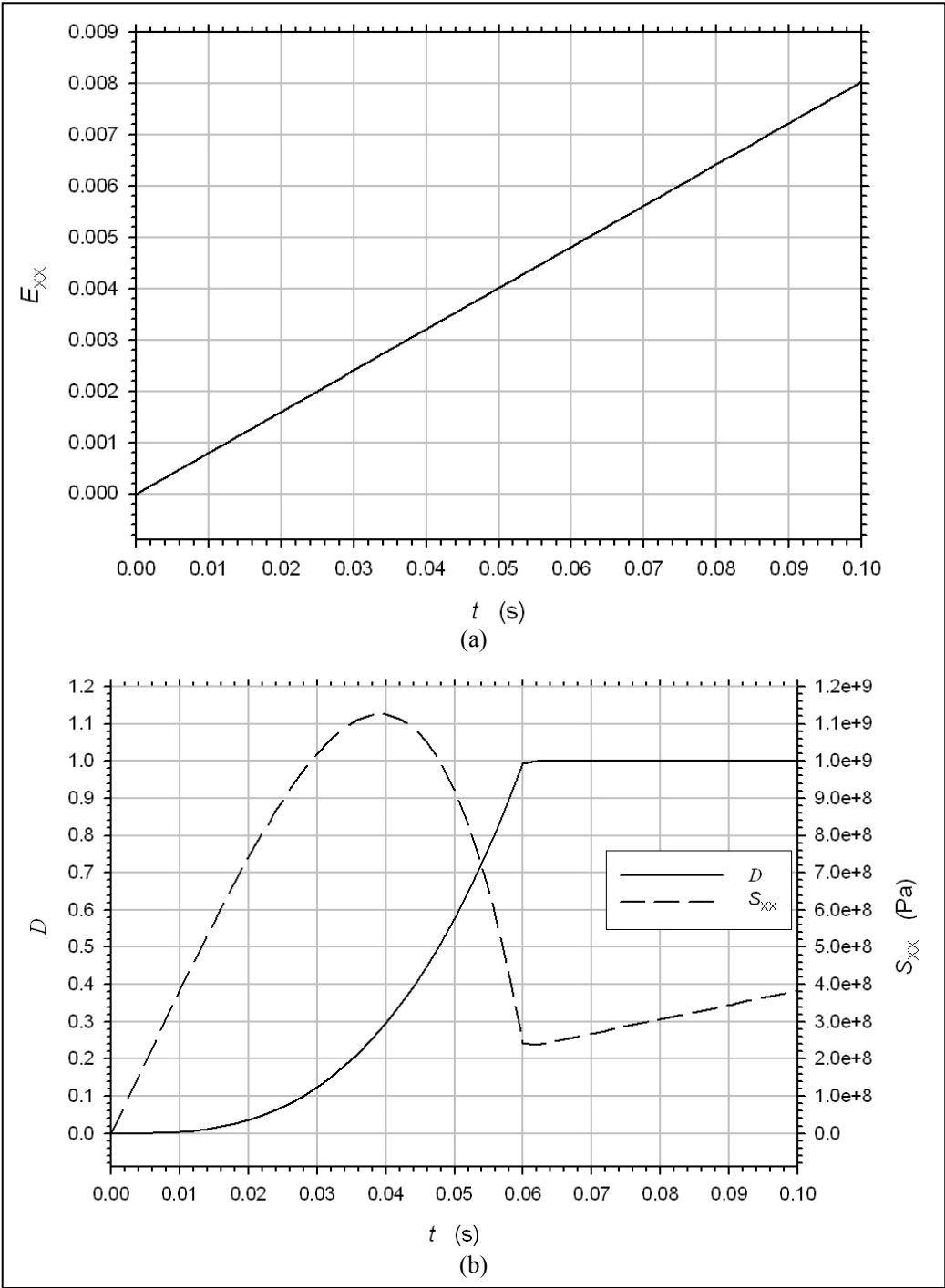


Figure 4. (a) The element in figure 3 is stretched at a constant positive (tensile) rate, and (b) D and S_{xx} evolve.

Table 1. Parameter values used in figure 4.

ρ (kg/m ³)	3215.
μ (GPa)	193.0
ν	0.1606
C (m·s/kg)	1.0×10^{-5}
ϕ_{\min}	0.1
L_0 (m)	0.01
v_0 (m/s)	8.0×10^{-4}

In figure 5, equation 40 for S_{XX} is evaluated for the case of no damage ($C = 0$), and the result is compared with the previous evaluation for $C = 1.0 \times 10^{-5}$ m·s/kg. We see that the damage model has substantially reduced the stress levels attained.

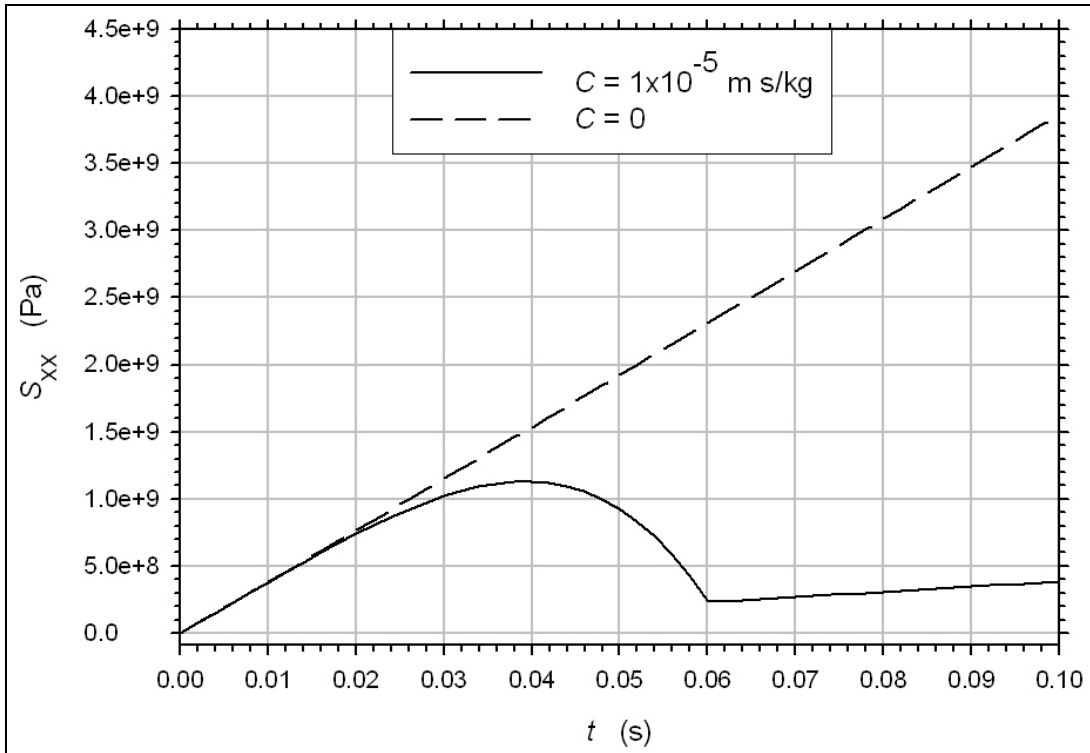


Figure 5. The solution to the problem in figure 3 evaluated with and without damage.

3.3.2 Uniaxial Compression at a Constant Stretch Rate

Next, the direction of v_0 in figure 3 is reversed so that a constant stretch-rate uniaxial compression test is performed. Figure 6 shows the results for D and S_{XX} vs. t .

The D results in figure 6 are identical to those in figure 4 from the tension test. Equation 35 is quadratic in strain rate and so does not distinguish tension from compression. Ultimately, this feature stems from the hypothesis of the damage model that the rate of damage growth is proportional to the strain energy, which is quadratic in the strain components.

Nevertheless, the stresses that develop in the compression test are properly compressive. Note that, for a given absolute value of E_{XX} , the value of S_{XX} in figure 6 is equal in magnitude and opposite in sign to its counterpart in figure 4.

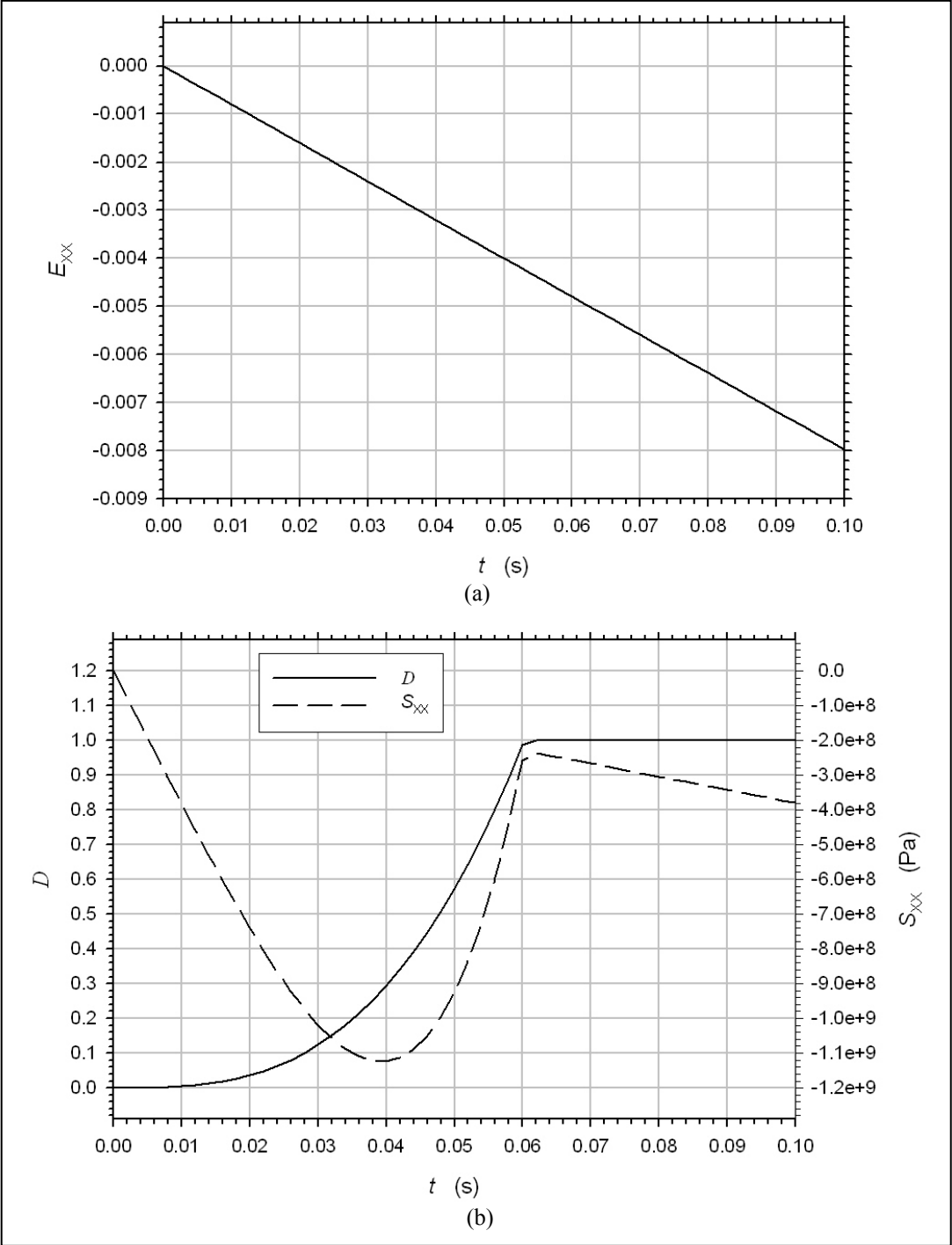


Figure 6. (a) The element in figure 3 is compressed at a constant negative stretch rate, and (b) D and S_{XX} evolve.

4. Application to Normal Plate-on-Plate Impact

4.1 The Initial Value, Boundary Value Problem

In normal plate-on-plate impact, a flyer plate is launched at a certain velocity into a stationary target plate. If the flyer and target plates are composed of the same material, the impact is said to be “symmetric.”

At time $t = 0$, let the origin of our stationary coordinate system lie at the center of the impacted face of the target plate. Let the x axis be orthogonal to that surface and be directed into the target. That is, at $t = 0$, $x = 0$ defines the impacted face of the target plate and $x = L$, where L is the initial thickness of the target plate, defines the free surface, the motion of which can be measured with the VISAR technique. The y and z axes of the Cartesian coordinate system lie in the impacted face of the target plate.

In the central portion of the target plate, i.e., the region of sufficiently small y and z so as not yet to be affected by unloading waves from the lateral edges, a condition of uniaxial strain is closely satisfied. Let u_x , u_y , and u_z be the three components of displacement. Throughout the central portion of the target plate,

$$u_y \equiv u_z \equiv 0 \quad (41a)$$

$$\frac{\partial u_x}{\partial y} \equiv \frac{\partial u_x}{\partial z} \equiv 0 \quad (41b)$$

The components of the infinitesimal strain tensor \mathbf{e} are related to displacement components by equation 2. The condition of uniaxial strain requires that

$$e_{yy} \equiv e_{zz} \equiv e_{xy} \equiv e_{yz} \equiv e_{zx} \equiv 0 \quad (42a)$$

The only component of strain not identically zero is related to the displacement field by

$$e_{xx} = \frac{\partial u_x}{\partial x} \quad (42b)$$

Equations 14a–f determine the components of stress.

$$\sigma_{xx} = \phi(D) \cdot \frac{2(1-\nu)\mu}{1-2\nu} e_{xx} \quad (43a)$$

$$\sigma_{yy} = \sigma_{zz} = \phi(D) \cdot \frac{2\nu\mu}{1-2\nu} e_{xx} \quad (43b)$$

$$\sigma_{xy} \equiv \sigma_{yz} \equiv \sigma_{zx} \equiv 0 \quad (43c)$$

Equation 8 for damage evolution reduces to

$$\frac{\partial D}{\partial t} = (1 - \phi_{\min}) C \cdot \frac{(1 - \nu)\mu}{1 - 2\nu} \cdot e_{xx}^2 \quad (44)$$

To this we add the Cauchy x -momentum equation

$$\rho \frac{\partial^2 u_x}{\partial t^2} = \frac{\partial \sigma_{xx}}{\partial x} \quad (45)$$

The boundary conditions are sketched in figure 7a. On the impacted face at $x = 0$, a time-independent velocity v_0 is prescribed. On the free surface at $x = L$, zero normal stress is prescribed. Homogeneous initial conditions are imposed on displacement, velocity, and damage D .

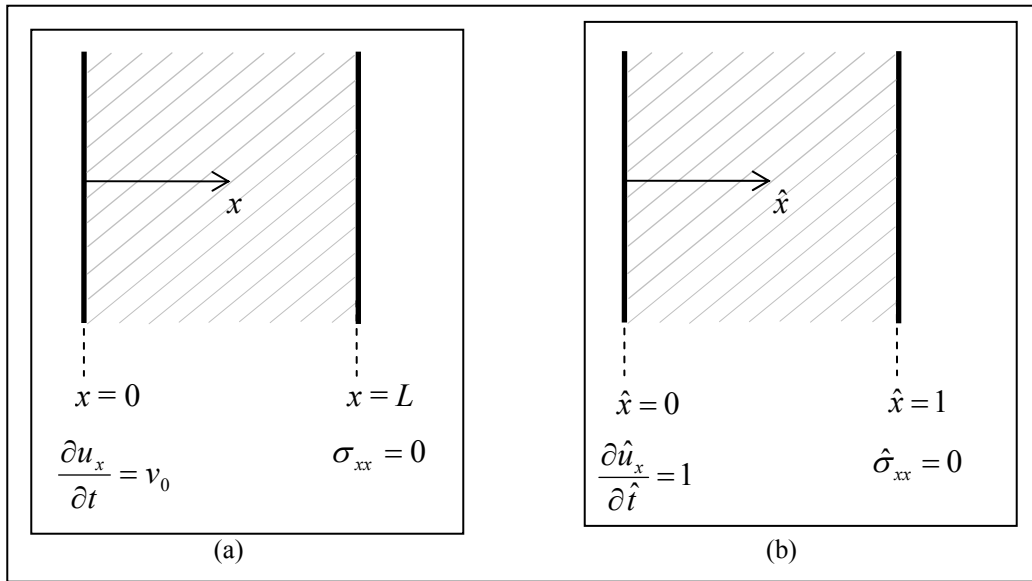


Figure 7. The boundary conditions imposed on the target in the uniaxial strain model of normal plate-on-plate impact (a) before and (b) after scaling.

Equations 42b, 43a, 44, and 45 are combined to yield two coupled nonlinear partial differential equations in two unknowns, u_x and D . These equations and the boundary and initial conditions constitute the following IVBVP. In all that follows, “DE,” “BC,” and “IC” denote “differential equations,” “boundary conditions,” and “initial conditions.”

DE

$$\frac{1}{c_0^2} \frac{\partial^2 u_x}{\partial t^2} = \frac{\partial^2 u_x}{\partial x^2} - (1 - \phi_{\min}) \left(D \frac{\partial^2 u_x}{\partial x^2} + \frac{\partial D}{\partial x} \frac{\partial u_x}{\partial x} \right) \quad (46)$$

$$\frac{\partial D}{\partial t} = (1 - \phi_{\min}) C \cdot \frac{(1 - \nu)\mu}{1 - 2\nu} \left(\frac{\partial u_x}{\partial x} \right)^2 \quad (47)$$

BC

$$\frac{\partial u_x}{\partial t}(0,t) = v_0, \quad \frac{\partial u_x}{\partial x}(L,t) = 0 \quad (48)$$

IC

$$u_x(x,0) = 0, \quad \frac{\partial u_x}{\partial t}(x,0) = 0, \quad D(x,0) = 0 \quad (49)$$

The domain is

$$x \in [0, L], \quad t \geq 0 \quad (50)$$

The parameter c_0 appearing in equation 46 is defined by

$$c_0 = \sqrt{\frac{2(1-\nu)\mu}{(1-2\nu)\rho}} \quad (51)$$

In an undamaged, isotropic, linearly elastic material, c_0 would correspond to the “longitudinal wave speed” or “dilatational wave speed” (see Kolsky 1963, pp. 10–15).

4.2 Scaling the IVBVP

The dimensionless quantities \hat{x} , \hat{t} , \hat{u}_x , \hat{v}_x , and $\hat{\sigma}_{xx}$ are defined by

$$\hat{x} = \frac{x}{L}, \quad \hat{t} = \frac{c_0 t}{L}, \quad \hat{u}_x = \frac{c_0 u_x}{v_0 L}, \quad \hat{v}_x = \frac{v_x}{v_0}, \quad \hat{\sigma}_{xx} = \frac{\sigma_{xx}}{\rho c_0 v_0} \quad (52)$$

These are substituted into equations 46 through 50 to yield the scaled IVBVP

DE

$$\frac{\partial^2 \hat{u}_x}{\partial \hat{t}^2} = \frac{\partial^2 \hat{u}_x}{\partial \hat{x}^2} - (1 - \phi_{\min}) \left(D \frac{\partial^2 \hat{u}_x}{\partial \hat{x}^2} + \frac{\partial D}{\partial \hat{x}} \frac{\partial \hat{u}_x}{\partial \hat{x}} \right) \quad (53)$$

$$\frac{\partial D}{\partial \hat{t}} = \Pi \cdot \left(\frac{\partial \hat{u}_x}{\partial \hat{x}} \right)^2 \quad (54)$$

BC

$$\frac{\partial \hat{u}_x}{\partial \hat{t}}(0, \hat{t}) = 1, \quad \frac{\partial \hat{u}_x}{\partial \hat{x}}(1, \hat{t}) = 0 \quad (55)$$

IC

$$\hat{u}_x(\hat{x}, 0) = 0, \quad \frac{\partial \hat{u}_x}{\partial \hat{t}}(\hat{x}, 0) = 0, \quad D(\hat{x}, 0) = 0 \quad (56)$$

$$\hat{x} \in [0, 1], \quad \hat{t} \geq 0 \quad (57)$$

in which

$$\Pi = (1 - \phi_{\min}) C \cdot \frac{\rho}{2c_0} \cdot L \cdot v_0^2 \quad (58)$$

This scaled IVBVP involves only two dimensionless parameters, ϕ_{\min} and Π . When we obtain solutions to this IVBVP, parameters C , μ , ν , L , and v_0 do not have to be varied independently but only in the combination Π ; Π is proportional to C and is a dimensionless measure of the material's damage sensitivity.

4.3 Dimensionless Parameter Π

For soda lime glass, Brar and Bless (1992) give $\rho = 2500 \text{ kg/m}^3$ and $c_0 = 5840 \text{ m/s}$. The factor $(\rho/2c_0)$ for this material is $0.214 \text{ kg}\cdot\text{s/m}^4$.

Choose $\phi_{\min} = 0.1$. From equation 58, we have

$$\Pi \approx 0.193 \frac{\text{kg}\cdot\text{s}}{\text{m}^4} \cdot C \cdot L \cdot v_0^2$$

The target plate thickness is typically a few millimeters, so $L \approx 0.005 \text{ m}$. One-half the flyer plate speed is typically a few hundred meters per second, so $v_0 \approx 300 \text{ m/s}$. Thus,

$$\Pi \approx 86.7 \frac{\text{kg}}{\text{m}\cdot\text{s}} \cdot C \quad (59)$$

4.4 Analytical Solution for the Case of No Damage ($\Pi = 0$)

For $\Pi = 0$,

$$\frac{\partial D_0}{\partial \hat{t}} \equiv 0 \quad (60)$$

and the IVBVP reduces to

DE

$$\frac{\partial^2 \hat{u}_0}{\partial \hat{t}^2} = \frac{\partial^2 \hat{u}_0}{\partial \hat{x}^2} \quad (61)$$

BC

$$\frac{\partial \hat{u}_0}{\partial \hat{t}}(0, \hat{t}) = 1, \quad \frac{\partial \hat{u}_0}{\partial \hat{x}}(1, \hat{t}) = 0 \quad (62)$$

IC

$$\hat{u}_0(\hat{x}, 0) = 0, \quad \frac{\partial \hat{u}_0}{\partial \hat{t}}(\hat{x}, 0) = 0 \quad (63)$$

A separation of variables procedure leads to the Fourier series solution

$$\hat{u}_0(\hat{x}, \hat{t}) = \hat{t} - \frac{8}{\pi^2} \sum_{n=1}^{\infty} \frac{1}{(2n-1)^2} \cdot \sin\left[\frac{(2n-1)\pi\hat{x}}{2}\right] \cdot \sin\left[\frac{(2n-1)\pi\hat{t}}{2}\right] \quad (64)$$

This solution can be obtained in a more convenient form by means of Laplace transforms. Let $L[f(\hat{x}, \hat{t})]$ denote the Laplace transform of $f(\hat{x}, \hat{t})$. This operation is defined by

$$L[f(\hat{x}, \hat{t})] \equiv \int_0^{\infty} f(\hat{x}, \hat{t}) e^{-s\hat{t}} d\hat{t} \quad (65)$$

The application of this operation to equations 61 and 62 yields the transformed BVP

DE

$$\frac{\partial^2 U(\hat{x}, s)}{\partial \hat{x}^2} - s^2 U(\hat{x}, s) = 0 \quad (66)$$

BC

$$U(0, s) = \frac{1}{s^2}, \quad \frac{\partial U(1, s)}{\partial \hat{x}} = 0 \quad (67)$$

in which $U(\hat{x}, s)$ denotes the Laplace transform of $\hat{u}_0(\hat{x}, \hat{t})$.

The solution of equation 66 subject to the boundary conditions 67 is

$$U(\hat{x}, s) = \frac{1}{s^2} \left[e^{-s\hat{x}} + e^{-s(2-\hat{x})} \right] \cdot \frac{1}{1 + e^{-2s}} \quad (68)$$

The Maclaurin expansion of the final factor is

$$\frac{1}{1 + e^{-2s}} = 1 - e^{-2s} + e^{-4s} + \dots$$

so that equation 68 can be written as

$$U(\hat{x}, s) = \frac{1}{s^2} \left[e^{-s\hat{x}} + e^{-s(2-\hat{x})} - e^{-s(2+\hat{x})} - \dots \right] \quad (69)$$

It is easily verified that

$$L[(\hat{t} - c_1 - c_2\hat{x}) \cdot H(\hat{t} - c_1 - c_2\hat{x})] = \frac{e^{-s(c_1 + c_2\hat{x})}}{s^2} \quad (70)$$

in which c_1 and c_2 are constants and $H(\hat{t} - c_1 - c_2\hat{x})$, the Heaviside unit step function of the argument, is defined by

$$H(\hat{t} - c_1 - c_2\hat{x}) \equiv \begin{cases} 1 & ; c_1 + c_2\hat{x} \leq \hat{t} \\ 0 & ; c_1 + c_2\hat{x} > \hat{t} \end{cases} \quad (71)$$

Therefore, the inverse Laplace transform of equation 69 is

$$\hat{u}_0(\hat{x}, \hat{t}) = (\hat{t} - \hat{x}) \cdot H(\hat{t} - \hat{x}) + (\hat{t} + \hat{x} - 2) \cdot H(\hat{t} + \hat{x} - 2) - (\hat{t} - \hat{x} - 2) \cdot H(\hat{t} - \hat{x} - 2) \quad (72)$$

in which $\hat{t} \in [0, 3]$.

Each term in this d'Alembert form of the solution corresponds to a reflection of the shock. The solution is truncated after three terms because the phenomenon depicted in figure 1 should likely occur during $\hat{t} \in [1, 2]$ and almost definitely before $\hat{t} = 3$. In dimensional form, equation 72 becomes

$$u_0(x, t) = \frac{v_0}{c_0} \left\{ (c_0 t - x) \cdot H(c_0 t - x) + (c_0 t + x - 2L) \cdot H(c_0 t + x - 2L) - (c_0 t - x - 2L) \cdot H(c_0 t - x - 2L) \right\} \quad (73)$$

in which $t \in [0, 3L/c_0]$.

4.5 Perturbation Procedure for the Case of Small Π

If the dimensionless group Π is small, then an approximate solution to the IVBVP of equations 53 through 57 can be obtained if we perturb about the equation 72 solution for zero Π . That is, let

$$\hat{u}_x = \hat{u}_0 + \hat{u}_1 \cdot \Pi + O(\Pi^2) \quad (74a)$$

$$D = D_1 \cdot \Pi + O(\Pi^2) \quad (74b)$$

If we substitute these expansions into equations 53 through 56 and collect terms of $O(\Pi)$, DE

$$\frac{\partial^2 \hat{u}_1}{\partial \hat{t}^2} = \frac{\partial^2 \hat{u}_1}{\partial \hat{x}^2} - (1 - \phi_{\min}) \left(D_1 \frac{\partial^2 \hat{u}_0}{\partial \hat{x}^2} + \frac{\partial D_1}{\partial \hat{x}} \frac{\partial \hat{u}_0}{\partial \hat{x}} \right) \quad (75)$$

$$\frac{\partial D_1}{\partial \hat{t}} = \left(\frac{\partial \hat{u}_0}{\partial \hat{x}} \right)^2 \quad (76)$$

BC

$$\frac{\partial \hat{u}_1}{\partial \hat{t}}(0, \hat{t}) = 0, \quad \frac{\partial \hat{u}_1}{\partial \hat{x}}(1, \hat{t}) = 0 \quad (77)$$

IC

$$\hat{u}_1(\hat{x}, 0) = 0, \quad \frac{\partial \hat{u}_1}{\partial \hat{t}}(\hat{x}, 0) = 0, \quad D_1(\hat{x}, 0) = 0 \quad (78)$$

Equations 72, 76, and 78c can be used to determine D_1 . From equation 72,

$$\frac{\partial \hat{u}_0(\hat{x}, \hat{t})}{\partial \hat{x}} = -H(\hat{t} - \hat{x}) + H(\hat{t} + \hat{x} - 2) + H(\hat{t} - \hat{x} - 2)$$

so that

$$\left(\frac{\partial \hat{u}_0(\hat{x}, \hat{t})}{\partial \hat{x}} \right)^2 = H(\hat{t} - \hat{x}) - H(\hat{t} + \hat{x} - 2) - 3H(\hat{t} - \hat{x} - 2)$$

The result is

$$D_1(\hat{x}, \hat{t}) = (\hat{t} - \hat{x}) \cdot H(\hat{t} - \hat{x}) - (\hat{t} + \hat{x} - 2) \cdot H(\hat{t} + \hat{x} - 2) - 3(\hat{t} - \hat{x} - 2) \cdot H(\hat{t} - \hat{x} - 2) \quad (79)$$

in which $\hat{t} \in [0, 3)$. Our solution for D , valid to $O(\Pi)$, is then

$$D(\hat{x}, \hat{t}) = [(\hat{t} - \hat{x}) \cdot H(\hat{t} - \hat{x}) - (\hat{t} + \hat{x} - 2) \cdot H(\hat{t} + \hat{x} - 2) - 3(\hat{t} - \hat{x} - 2) \cdot H(\hat{t} - \hat{x} - 2)] \cdot \Pi + O(\Pi^2) \quad (80)$$

The dimensional form of equation 80 is

$$D(x, t) \cong (1 - \phi_{\min}) C \cdot \frac{\rho v_0^2}{2c_0} \left[(c_0 t - x) \cdot H(c_0 t - x) + (c_0 t + x - 2L) \cdot H(c_0 t + x - 2L) - 3(c_0 t - x - 2L) \cdot H(c_0 t - x - 2L) \right] \quad (81)$$

in which $t \in [0, 3L/c_0)$. Equation 80 is evaluated in figure 8 for Π of 0.1 and 0.3. The $O(\Pi)$ solution is linear in Π , so the solution in figure 8b is just a multiple of that in 8a.

A combination of equations 72, 75, and 79 leads to an inhomogeneous wave equation with a known forcing function. The equation can be solved for \hat{u}_1 , subject to the homogeneous boundary and initial conditions in equations 77 and 78.

4.6 LS-DYNA Results for Various Values of Π

The IVBVP in equations 53 through 57 can be solved for arbitrary Π by means of the LS-DYNA implementation described in section 3. Figure 9 shows the FE mesh that was employed. The length between $\hat{x} = 0$ and $\hat{x} = 1$ is divided into 16,000 eight-node brick elements. The uniaxial displacement condition of equation 41a was imposed by means of constraints on the boundary nodes. The IVBVP could have been modeled with a single row of elements; the 64 rows shown in figure 9 were used to obtain good visibility in the mesh plots while maintaining an element aspect ratio of one. Gaussian quadrature was performed with one integration point per element. Default artificial viscosity coefficients were used: quadratic viscosity $Q1 = 1.5$, linear viscosity $Q2 = 0.06$, hourglass coefficient $QH = 0.1$.

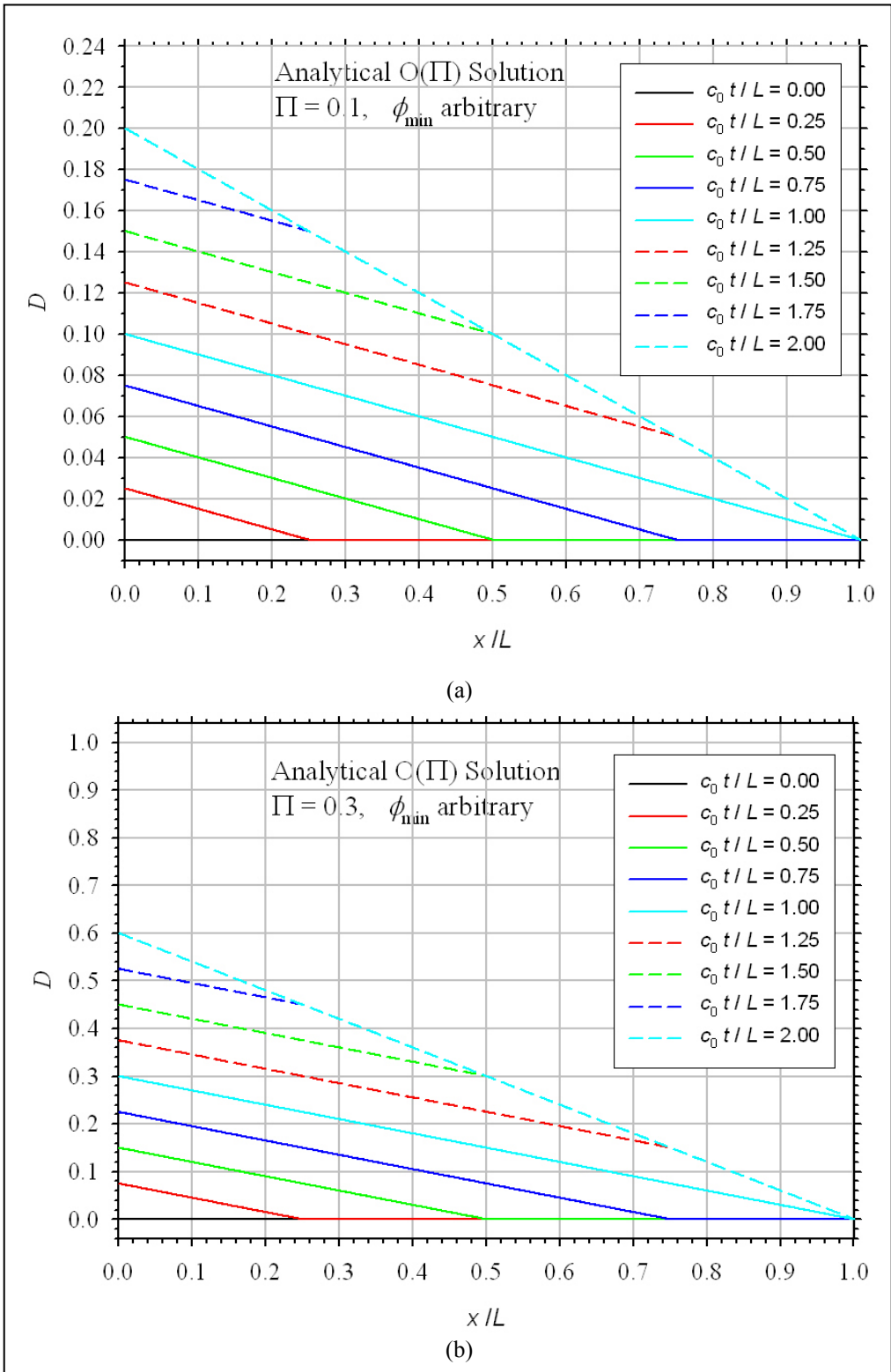


Figure 8. The analytical $O(\Pi)$ solution evaluated for (a) $\Pi = 0.1$ and (b) $\Pi = 0.3$.

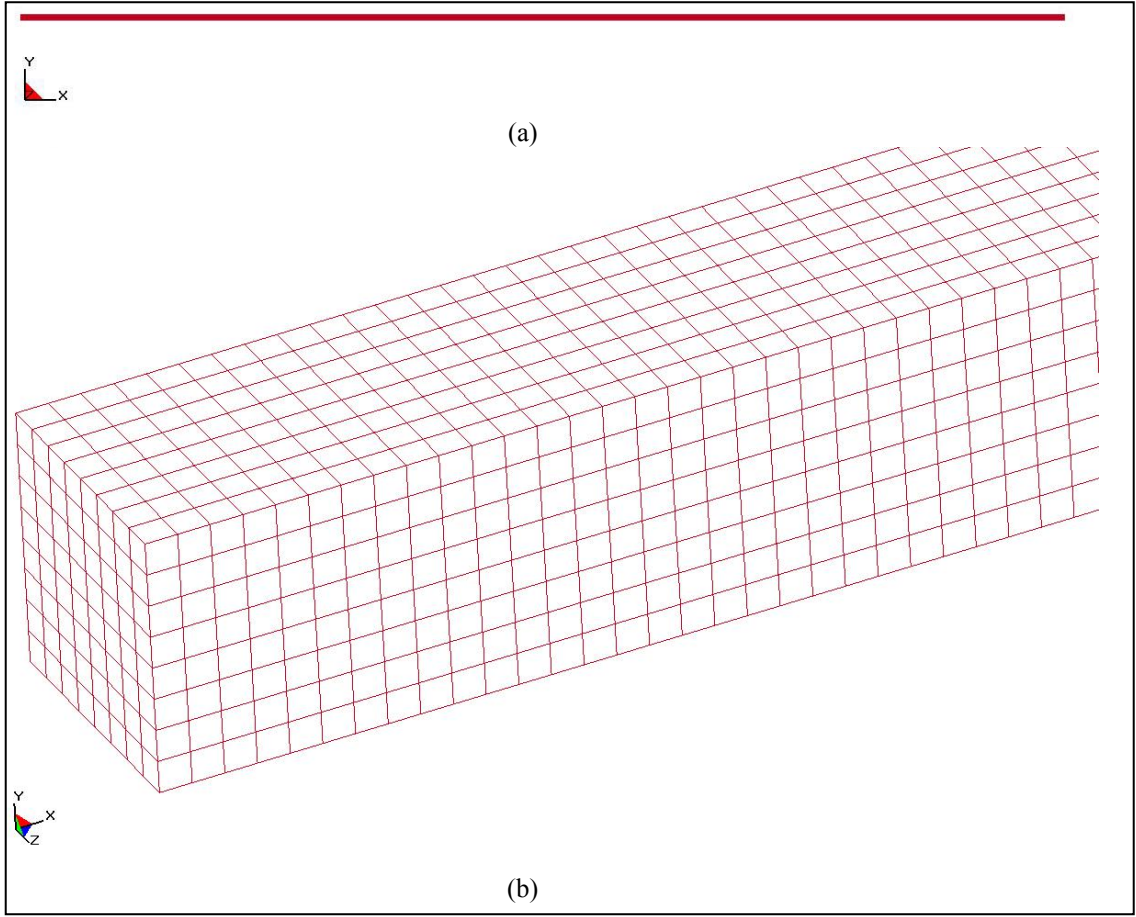


Figure 9. FE mesh for the target plate: (a) entire thickness of the plate, (b) the $x = 0$ end.

The solution was obtained for $\Pi = 0, 0.1, 0.2, 0.3,$ and $0.4,$ and for $\phi_{\min} = 0.1.$ Figure 10 shows the results for $\hat{v}_x(1, \hat{t}),$ the free-surface normal velocity as a function of time. The compressive shock arrives at $\hat{t} = 1.$ For $\Pi = 0,$ the scaled velocity jumps to 2 and remains at that level until $\hat{t} = 3.$ As Π is increased successively to 0.1, 0.2, 0.3, and 0.4, the free-surface velocity jumps at $\hat{t} = 1$ to ever-decreasing levels. Furthermore, for $\Pi > 0,$ the free-surface velocity does not remain constant throughout the duration $\hat{t} \in (1, 3).$ Table 2 compares $\hat{v}_x(1, \hat{t} = 1.125)$ and $\hat{v}_x(1, \hat{t} = 2.000).$ We see that

$$\hat{v}_x(1, \hat{t} = 2.000) > \hat{v}_x(1, \hat{t} = 1.125); \quad \Pi = 0.1, 0.2 \quad (82a)$$

$$\hat{v}_x(1, \hat{t} = 2.000) < \hat{v}_x(1, \hat{t} = 1.125); \quad \Pi = 0.3, 0.4 \quad (82b)$$

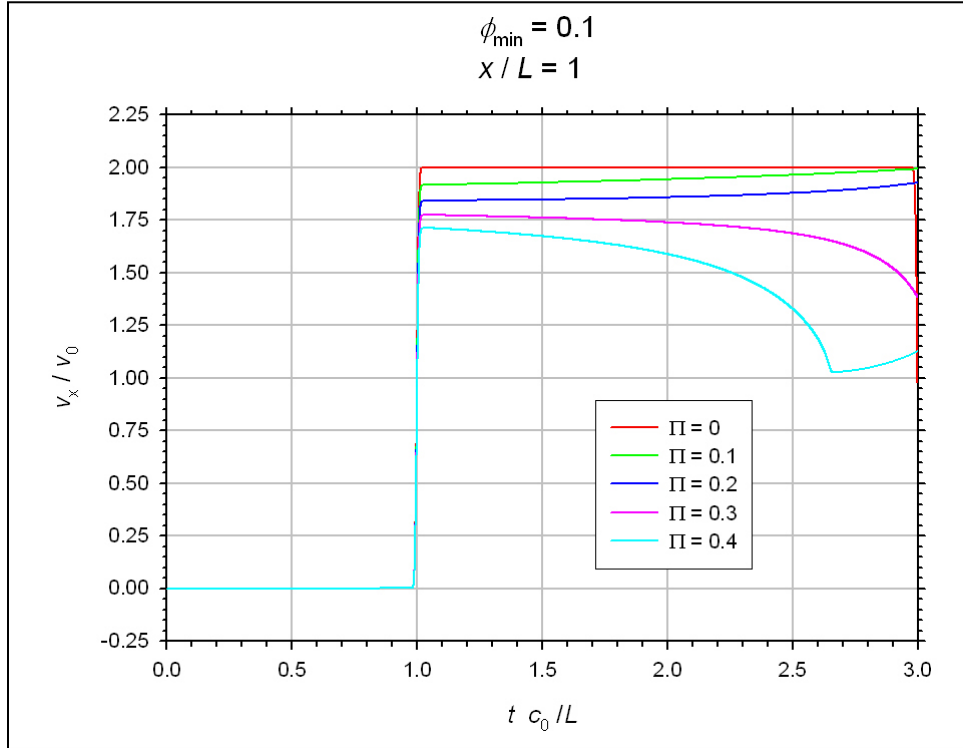


Figure 10. \hat{v}_x at $\hat{x} = 1$ (the free-surface normal velocity) as a function of \hat{t} and for various Π ($\phi_{\min} = 0.1$).

Table 2. The scaled free-surface velocity, \hat{v}_x at $\hat{x} = 1$, for $\hat{t} = 1.125$, $\hat{t} = 2.000$, and the difference between the two for various Π ($\phi_{\min} = 0.1$).

Π	$\hat{v}_x(\hat{x} = 1, \hat{t} = 1.125)$	$\hat{v}_x(\hat{x} = 1, \hat{t} = 2.000)$	$\hat{v}_x(1, 2.000) - \hat{v}_x(1, 1.125)$
0	2.00000	2.00000	0.00000
0.05	1.95846	1.97471	0.01626
0.1	1.91831	1.94310	0.02479
0.11	1.91051	1.93596	0.02545
0.12	1.90271	1.92849	0.02578
0.121	1.90189	1.92775	0.02586
0.122	1.90115	1.92701	0.02586
0.123	1.90033	1.92619	0.02586
0.124	1.89959	1.92545	0.02586
0.125	1.89885	1.92471	0.02586
0.126	1.89803	1.92389	0.02586
0.127	1.89729	1.92315	0.02586
0.128	1.89647	1.92233	0.02586
0.129	1.89573	1.92159	0.02586
0.130	1.89491	1.92077	0.02586
0.131	1.89417	1.92003	0.02586
0.132	1.89343	1.91921	0.02578
0.133	1.89261	1.91839	0.02578
0.14	1.88727	1.91273	0.02545
0.15	1.87964	1.90435	0.02471
0.2	1.84236	1.85764	0.01527
0.3	1.77184	1.73859	-0.03325
0.4	1.70665	1.58810	-0.11856

The slight increase in velocity with time for $\Pi = 0.1$ and 0.2 indicates the arrival of a partially reflected unloading wave. However, this velocity rise is gradual over time and the computed free-surface velocity does not exhibit the distinct second plateau of figure 1a.

Figure 11 shows the computed spatial distributions of D and ϕ through the target plate's thickness. These profiles are plotted at time $\hat{t} = 1.5$, chosen to estimate the time at which the unloading wave should encounter the damage front according to the hypothesis sketched in figure 1b. In figure 11, for a given value of Π , the D and ϕ profiles display a resemblance because of the linearity of their relationship in equation 6. Note that changes in ϕ are broadly distributed across the thickness and do not occur abruptly at a specific location. As a consequence, increases in \hat{v}_x at $\hat{x} = 1$ for $\Pi = 0.1$ and 0.2 occur only gradually with time according to this model.

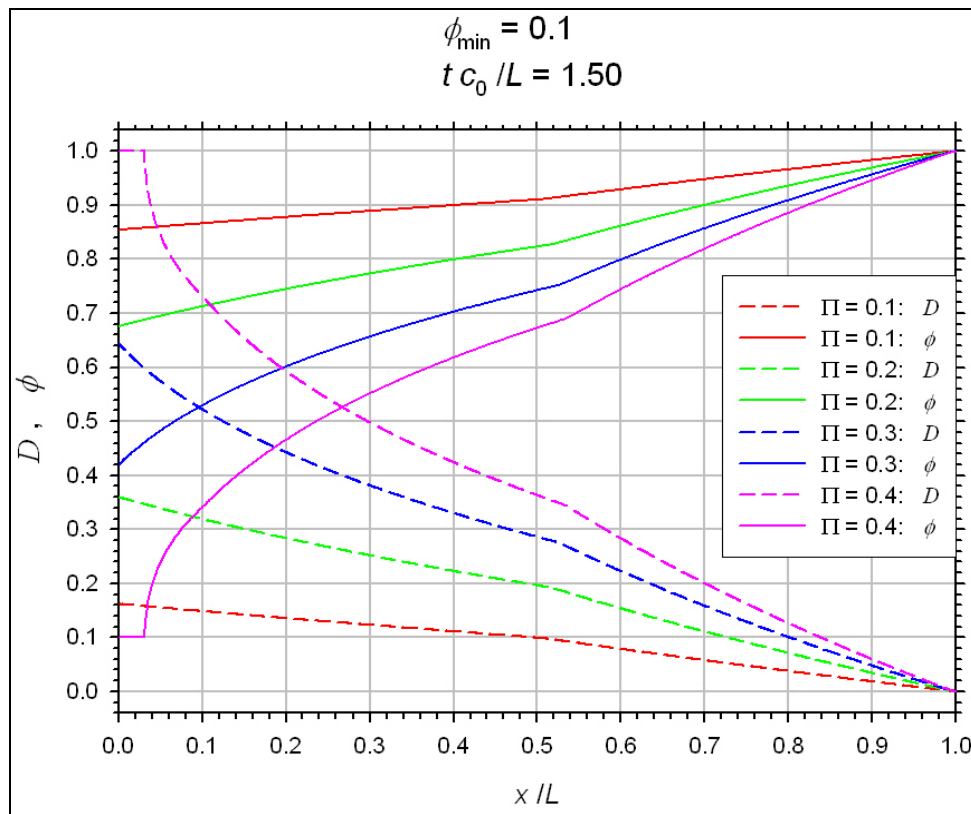


Figure 11. D and ϕ as functions of \hat{x} at $\hat{t} = 1.5$ and for various Π ($\phi_{\min} = 0.1$).

The solutions for $\Pi = 0.1$ and for $\Pi = 0.3$ are examined more closely in figures A-1 through A-9 of appendix A and figures B-1 through B-9 of appendix B, respectively.

Figures A-1 through A-3 and B-1 through B-3 show results for scaled stress $\hat{\sigma}_{xx}$. One effect of damage has been to *decrease the stress-wave speed*. For both $\Pi = 0.1$ and 0.3 , the compressive loading wave during $\hat{t} \in (0,1)$ traverses the undamaged target plate with a scaled speed very nearly equal to 1, but during $\hat{t} > 1$, the unloading wave travels back into the damaged material with a speed smaller than 1. Furthermore, this wave speed reduction is more pronounced at $\Pi = 0.3$ than at $\Pi = 0.1$. A second effect of damage has been to *decrease the amplitude of the stress*

signal, and this effect is also more pronounced at $\Pi = 0.3$ than at $\Pi = 0.1$. In figure B-1, note that the blue color lightens in the wake of the stress wave as early as $\hat{t} = 0.75$, indicating a substantial decrease (in absolute value) from the level of -1 that would pertain without damage. Figures A-1 and A-2 and figures B-1 and B-2 show through-thickness profiles of $\hat{\sigma}_{xx}$ at scaled-time intervals of 0.125. These figures further document the erosion over time of the absolute value of the compressive stress.

Figures A-4 through A-6 for $\Pi = 0.1$ and B-4 through B-6 for $\Pi = 0.3$ show results for D . These figures show that at a given \hat{x} , location D increases monotonically with time. Figures A-5 and B-5, which contain through-thickness profiles of D at fixed times, can be compared with figures 8a and 8b, respectively: the perturbation solution truncated at $O(\Pi)$ is useful at $\Pi = 0.1$ but grossly underpredicts D at $\Pi = 0.3$. In figures A-5 and B-5, we see that the through-thickness profiles of D do not exhibit steep fronts—a feature that was also noted in figure 11. Nevertheless, if we track the location at which D equals a specific constant between 0 and 1, that location drifts to ever-larger \hat{x} values over time until the unloading wave arrives to relieve the local strain energy. This is clearly seen in the $\hat{x} - \hat{t}$ plots in figures A-6 and B-6. These figures also display the location of the stress-wave front, which is identified with the location of the maximum value of $|d\hat{\sigma}_{xx}/d\hat{x}|$. Finally, figures A-6 and B-6 also depict the reduction in the stress-front's speed for $\hat{t} > 1$ by displaying the $(L - c_0 t)$ line.

Figures A-7 through A-9 and B-7 through B-9 present results for scaled velocity \hat{v}_x . Figures A-7 and B-7 show through-thickness profiles at \hat{t} intervals of 0.125 during $\hat{t} \in (0,1)$. Figures A-8, A-9, B-8, and B-9 show such profiles during $\hat{t} \in (1,2)$. Figures A-9 and B-9 are enlargements of A-8 and B-8, respectively, in the vicinity of the free surface at $\hat{x} = 1$. Figures A-9 and B-9 clearly show the increase in \hat{v}_x at $\hat{x} = 1$ with increasing time for $\Pi = 0.1$ and its decrease for $\Pi = 0.3$.

The IVBVP in equations 53 through 57 was then solved for additional values of Π . Figure 12 and table 2 present our results for the dependence of $[\hat{v}_x(\hat{x} = 1, \hat{t} = 2.000) - \hat{v}_x(\hat{x} = 1, \hat{t} = 1.125)]$ on Π . This quantity attains its maximum value at $\Pi = 0.126$. The solution for this value of Π is displayed in figures C-1 through C-7 of appendix C. This solution is qualitatively similar to that obtained for $\Pi = 0.1$.

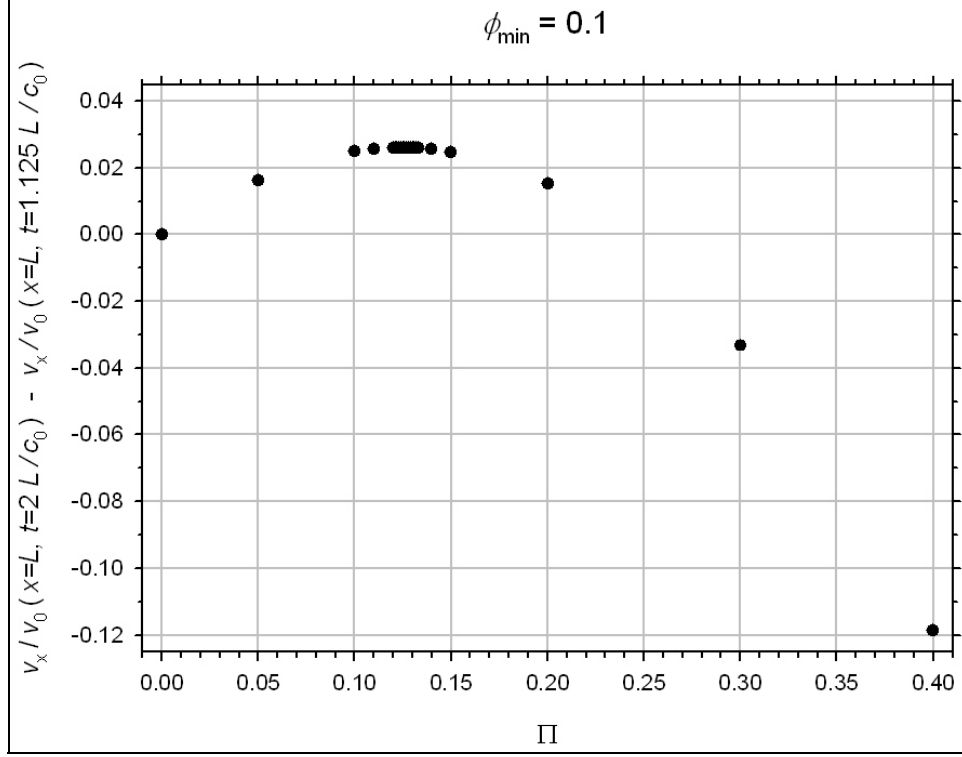


Figure 12. $\hat{v}_x(\hat{x} = 1, \hat{t} = 2.000) - \hat{v}_x(\hat{x} = 1, \hat{t} = 1.125)$ as a function of Π ($\phi_{\min} = 0.1$).

5. Conclusions

The damage model for brittle materials presented in Grinfeld and Wright (unpublished) and subsequently in Grinfeld et al. (in press) was installed in the LS-DYNA FE code. This damage model introduces a damage state variable D . The model consists of an evolution equation for D and a degradation function of D . The degradation function is applied multiplicatively to the elastic shear modulus of an isotropic linearly elastic material; Poisson ratio is unaltered.

The damage model was initially applied to the constant stretch-rate uniaxial tension and compression of a single eight-node brick finite element. We saw D and axial stress increase as a cubic and a quartic, respectively, with time. We also saw D attain the same value for a given absolute value of stretch, regardless whether that stretch involved tension or compression. Since the evolution equation is based on elastic strain energy (a quadratic function of the strain components), the damage model does not distinguish damage contributions from tension and compression. This issue can be addressed in a future refinement.

The model was then applied to simulations of normal plate-on-plate impact. We scaled the IVBVP and found the occurrence of only two dimensionless parameters, ϕ_{\min} and Π . The latter is a combination of pre-damaged elastic properties, material properties introduced by the damage

model, target geometry, and impact speed. Π is a measure of the material's damage sensitivity to elastic strain energy. The LS-DYNA implementation of the Grinfeld-Wright model was used to obtain solutions for the normal plate-on-plate impact problem for $\Pi = 0.1, 0.2, 0.3,$ and 0.4 . For smaller values of Π , a procedure for perturbing the $\Pi = 0$ (no damage) solution was outlined.

The LS-DYNA solutions for $\Pi = 0.1, 0.2, 0.3,$ and 0.4 were examined with regard to the failure wave hypothesis sketched in figure 1. For $\Pi = 0.1$ and 0.2 , the normal velocity of the target's free surface was seen to gradually increase slightly from its level associated with the initial arrival of the compressive shock. For $\Pi = 0.3$ and 0.4 , the free-surface velocity was seen to gradually decrease from its level associated with the initial arrival of the compressive shock. The solutions for damage and stress fields within the target revealed two competing mechanisms. The evolution of damage led to stiffness gradients within the target, which did indeed produce gradual reflections of the unloading wave back to the free surface. However, damage evolution also led to a reduction of the compressive stress field, which acted to reduce the free-surface velocity.

A proposed change in the Grinfeld-Wright model that might lead to the distinct recompression plateau in figure 1b is to replace the linear $\phi(D)$ relationship of equation 6. A more abrupt change of ϕ with D may achieve both goals of a more abrupt reflection of the loading wave and a smaller degradation in the stress amplitude of the unloading wave before the unloading wave encounters the abrupt change in ϕ .

6. References

- Brar, N. S.; Bless, S. J. Failure Waves in Glass Under Dynamic Recompression. *High Pressure Research* **1992**, *10*, 773–78.
- Coleman, B. D.; Gurtin, M. E. Thermodynamics with Internal State Variables. *The Journal of Chemical Physics* **1967**, *47*, 597–613.
- Grinfeld, M. A.; Schoenfeld, S. E.; Wright, T. W. Failure Fronts in Brittle Materials and Their Morphological Instabilities, *Shock Compression of Condensed Matter – 2005*, in press.
- Grinfeld, M. A.; Wright, T. W. *Thermodynamics of Brittle Fracture*, U.S. Army Research Laboratory: Aberdeen Proving Ground, MD, unpublished paper.
- Kanel, G. I.; Rasorenov, S. V.; Fortov, V. E. The Failure Waves and Spallations in Homogeneous Brittle Materials, *Shock Compression of Condensed Matter – 1991*, editors: Schmidt, S. C., Dick, R. D., Forbes, J. W., and Tasker, D. G., North-Holland: Amsterdam, pp. 451–454, 1992.
- Kolsky, H. *Stress Waves in Solids*, Dover: New York, 1963.
- Livermore Software Technology Corporation. *LS-DYNA Keyword User's Manual*. Version 970, Livermore, CA, April 2003.
- Malvern, L. E. *Introduction to the Mechanics of a Continuous Medium*, Prentice-Hall: Englewood Cliffs, NJ, 1969.

INTENTIONALLY LEFT BLANK

Appendix A. LS-DYNA Results for $\Pi = 0.1$

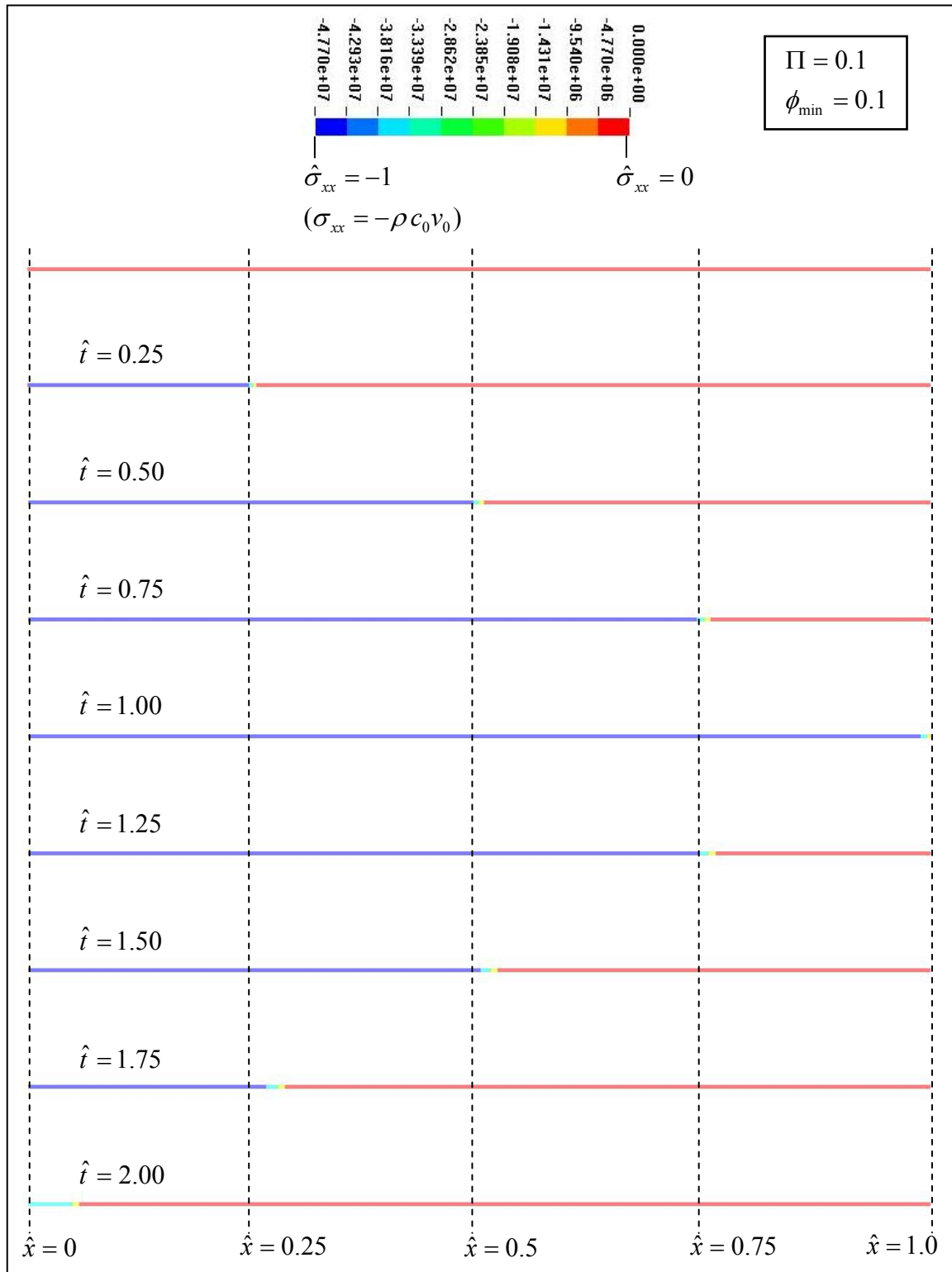


Figure A-1. Contours of $\hat{\sigma}_{xx}$ across the target plate for $\Pi = 0.1$ and $\phi_{\min} = 0.1$.

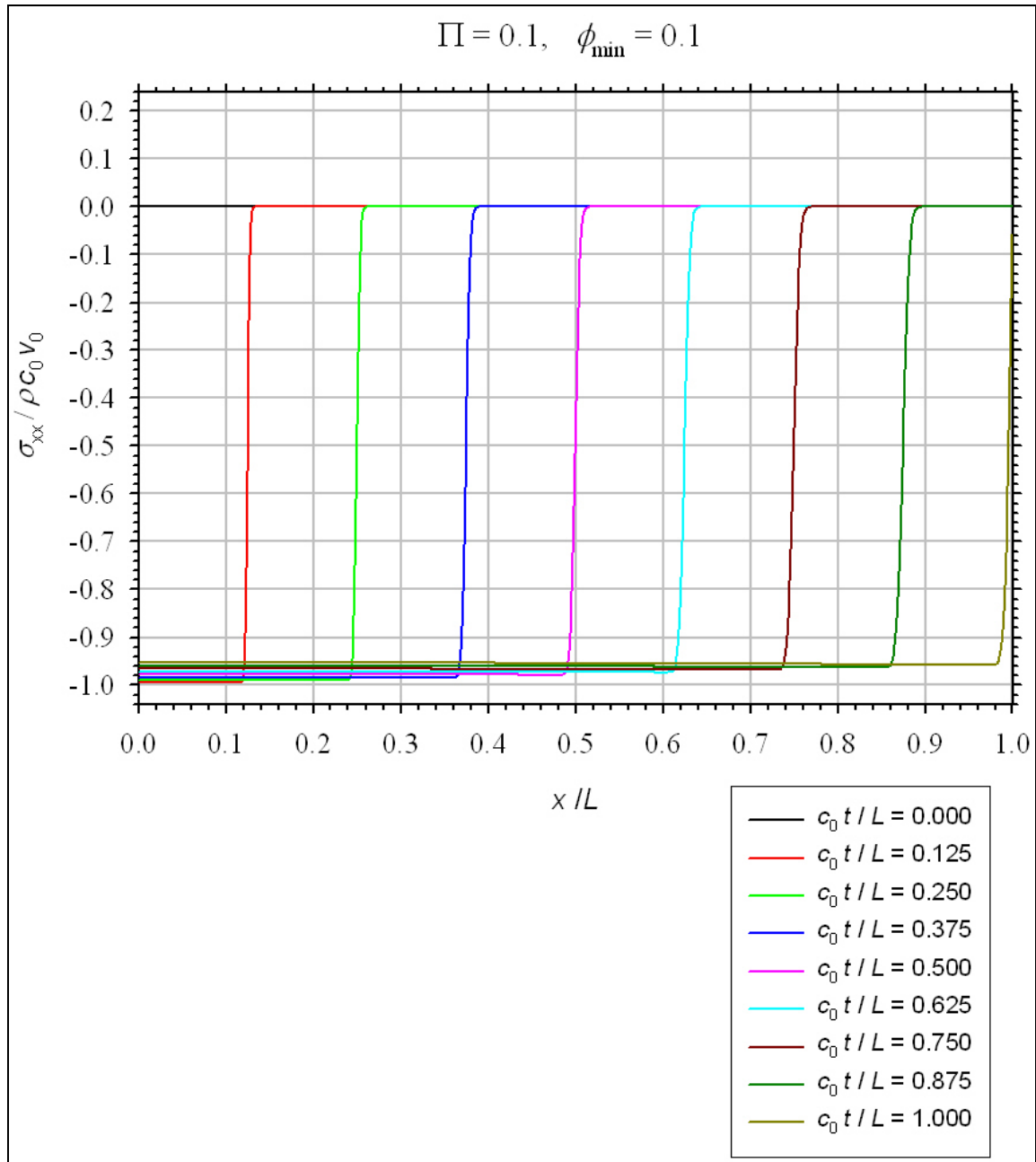


Figure A-2. $\hat{\sigma}_{xx}$ as functions of \hat{x} for various $\hat{t} \in [0,1]$ and for $\Pi = 0.1$. ($\phi_{\min} = 0.1$.)

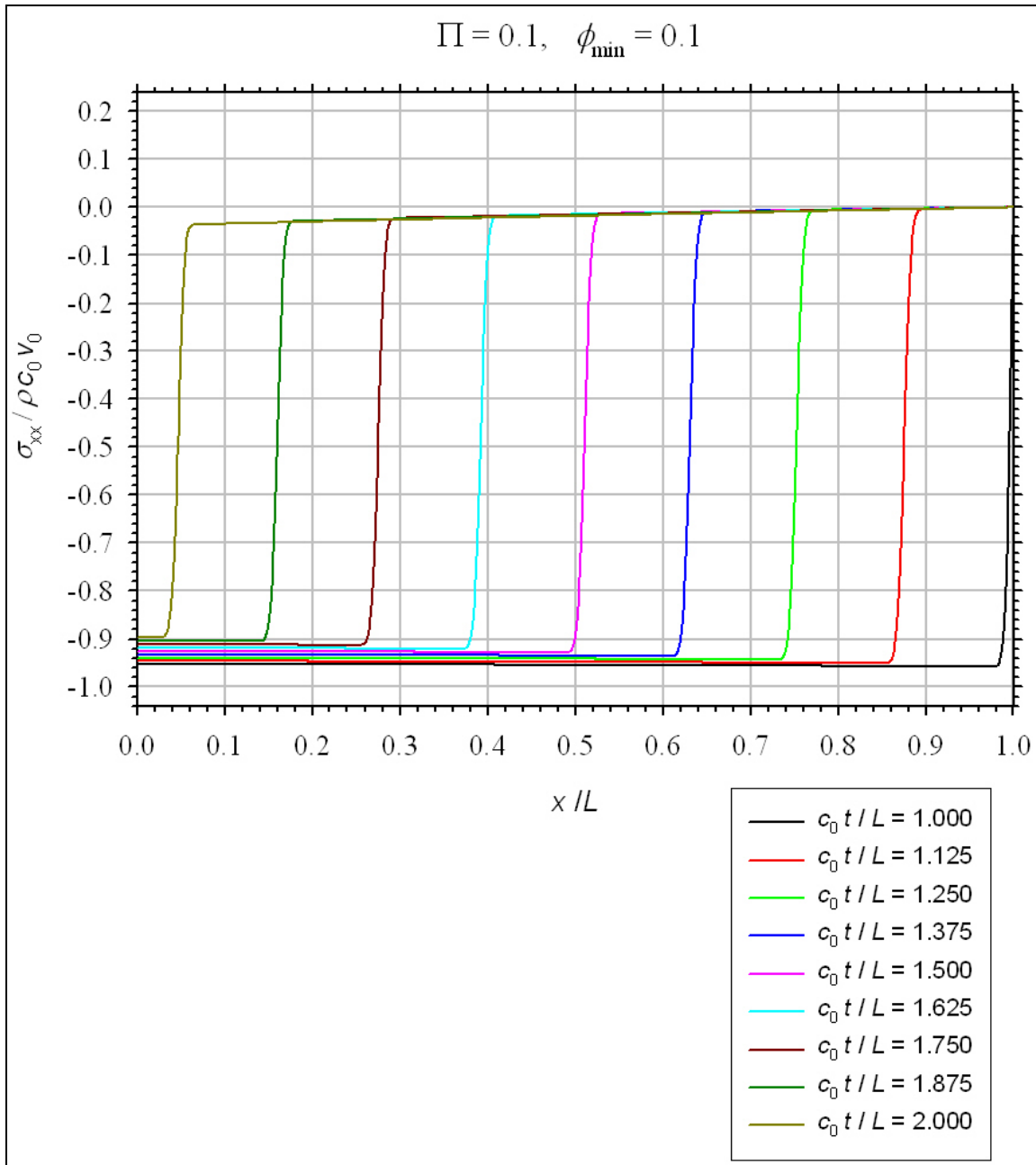


Figure A-3. $\hat{\sigma}_{xx}$ as functions of \hat{x} for various $\hat{t} \in [1,2]$ and for $\Pi = 0.1$. ($\phi_{\min} = 0.1$.)

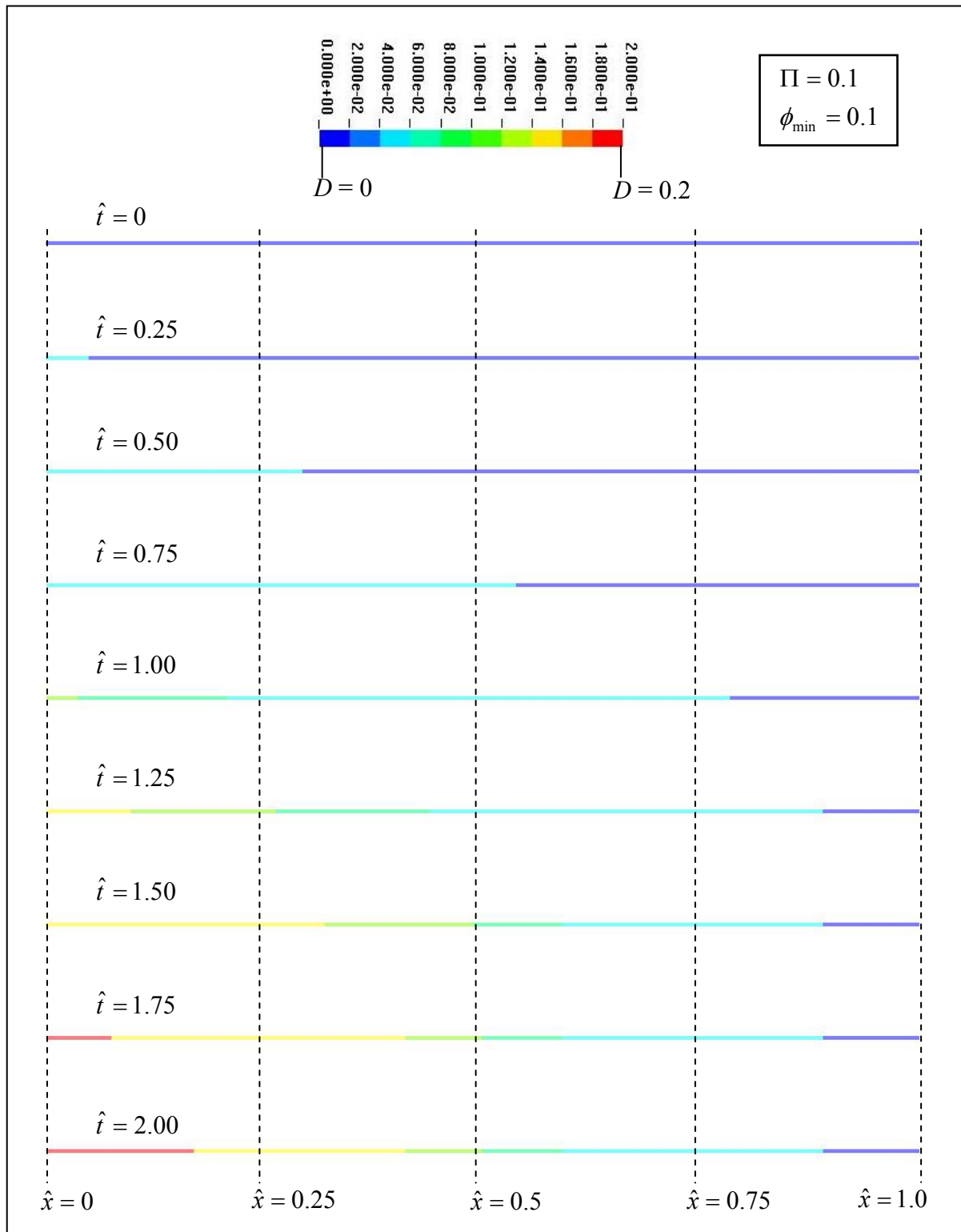


Figure A-4. Contours of D across the target plate for $\Pi = 0.1$ and $\phi_{\min} = 0.1$.

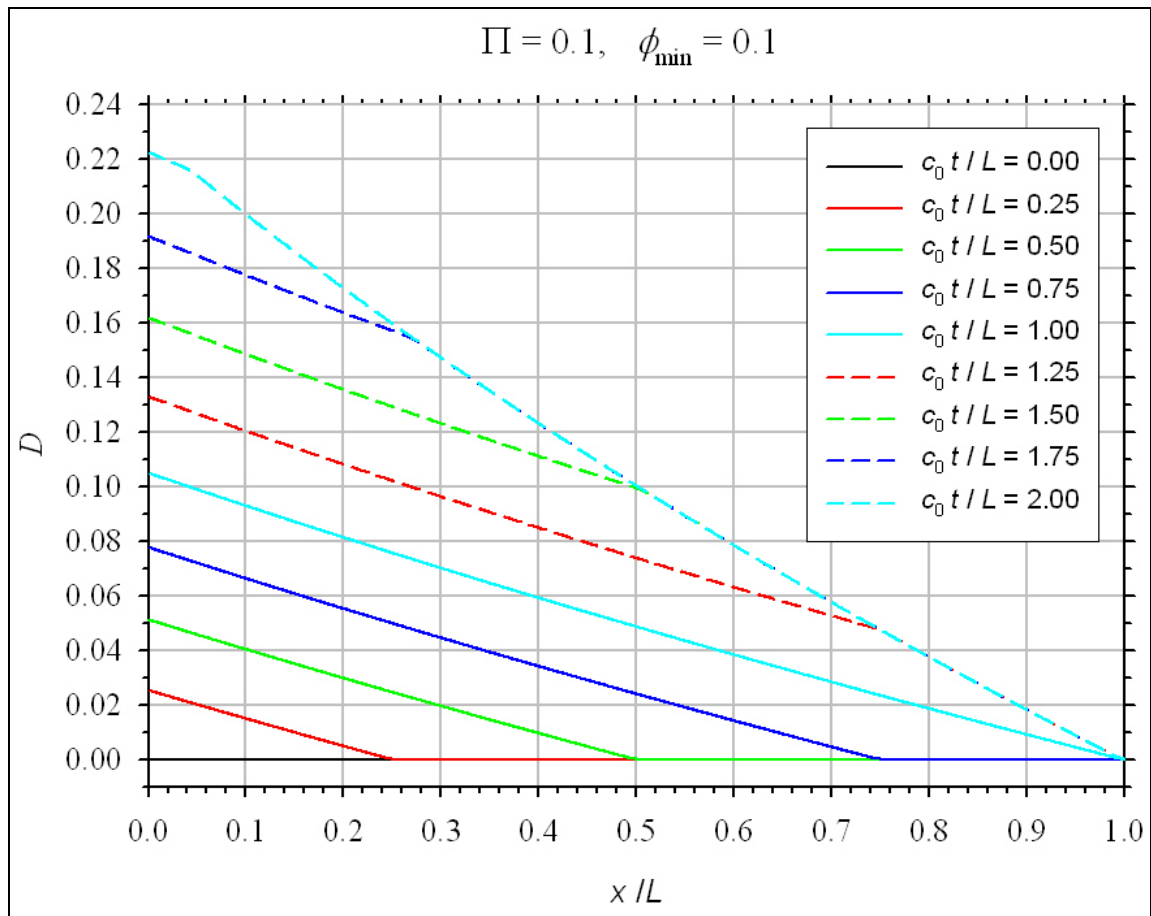


Figure A-5. D as functions of \hat{x} for various \hat{t} and for $\Pi = 0.1$. ($\phi_{\min} = 0.1$.)

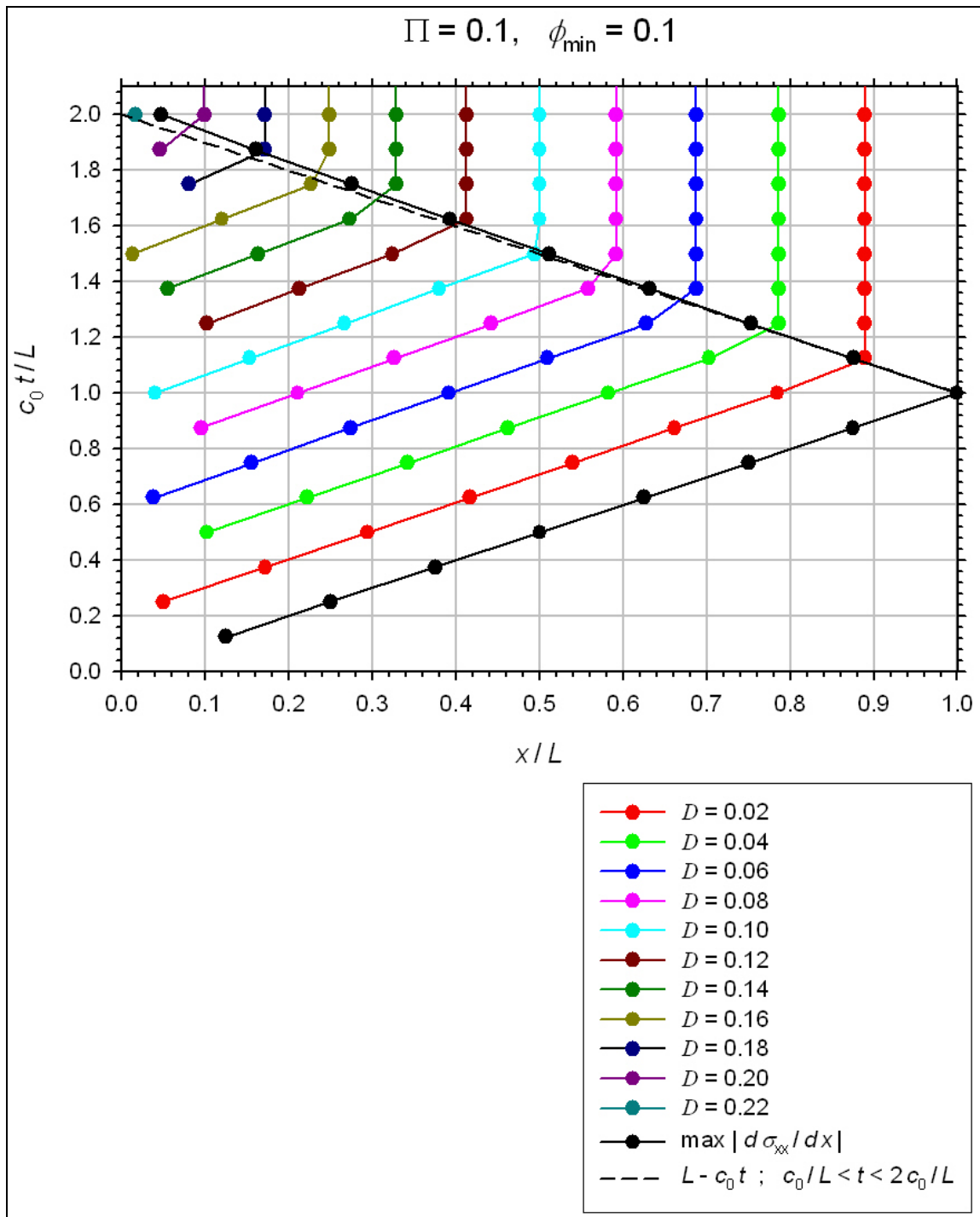


Figure A-6. D Contours in $\hat{x} - \hat{t}$ space for $\Pi = 0.1$. ($\phi_{\min} = 0.1$.)

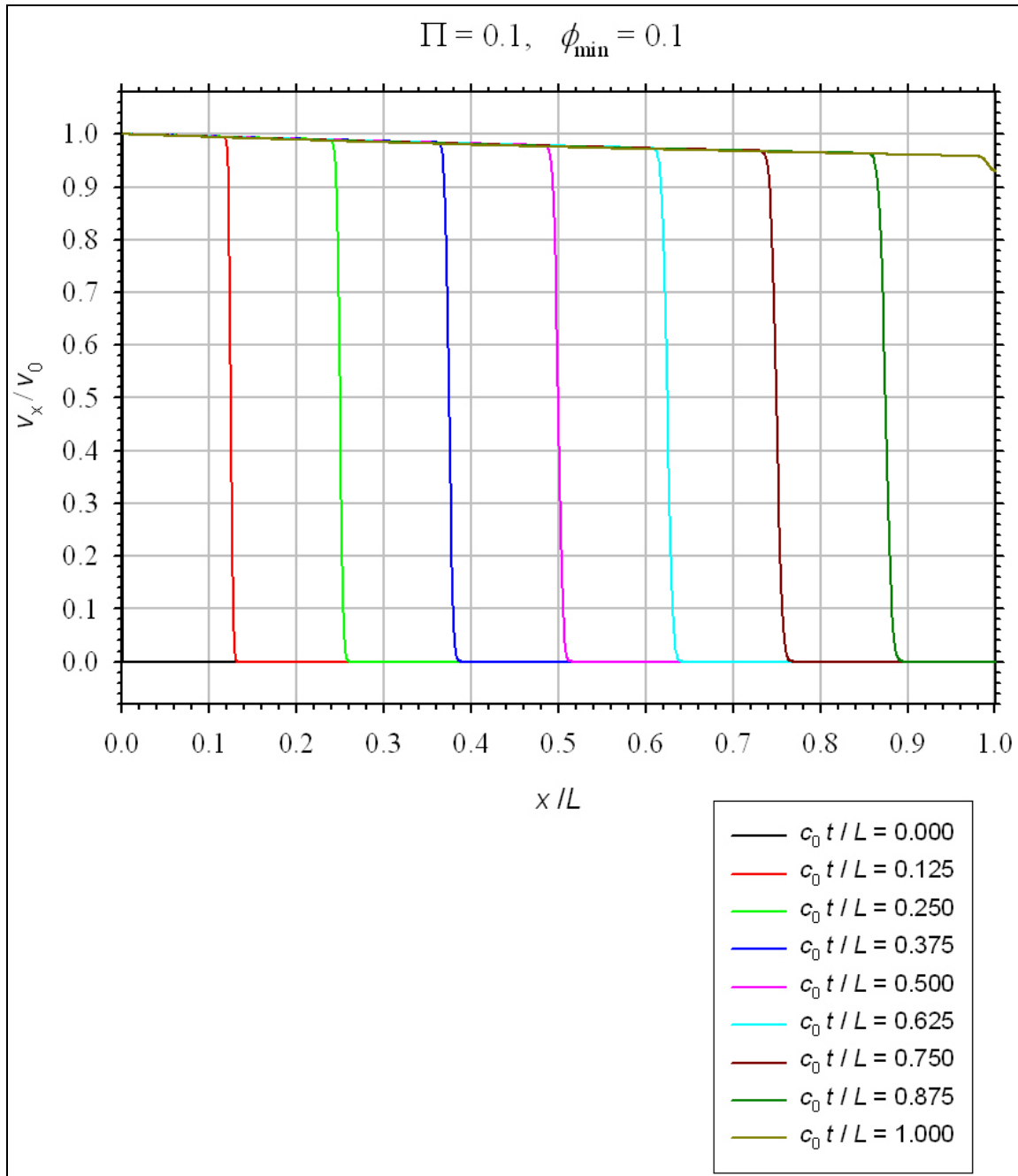


Figure A-7. \hat{v}_x as functions of \hat{x} for various $\hat{t} \in [0,1]$ and for $\Pi = 0.1$. ($\phi_{\min} = 0.1$.)

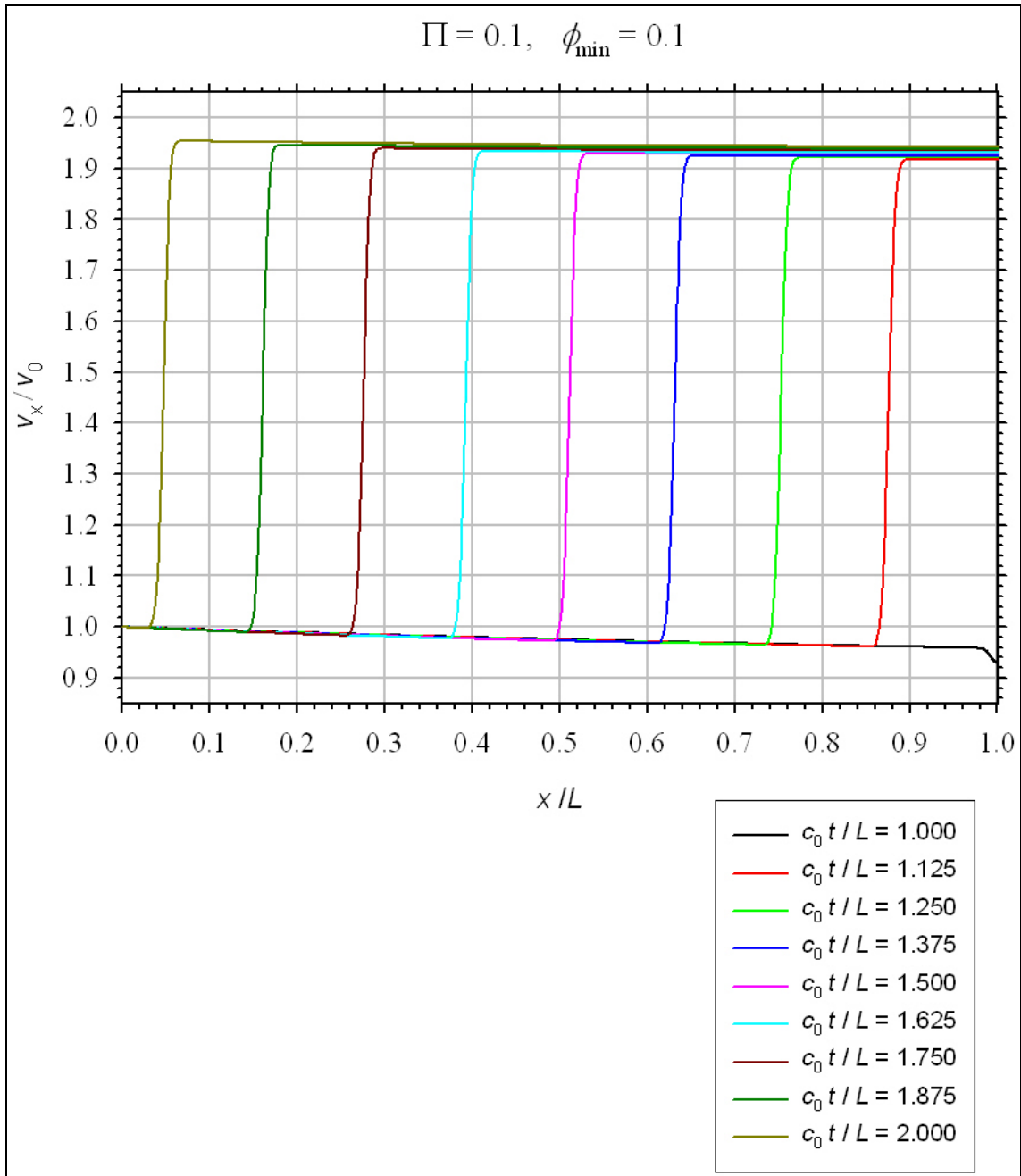


Figure A-8. \hat{v}_x as functions of \hat{x} for various $\hat{t} \in [1,2]$ and for $\Pi = 0.1$. ($\phi_{\min} = 0.1$.)

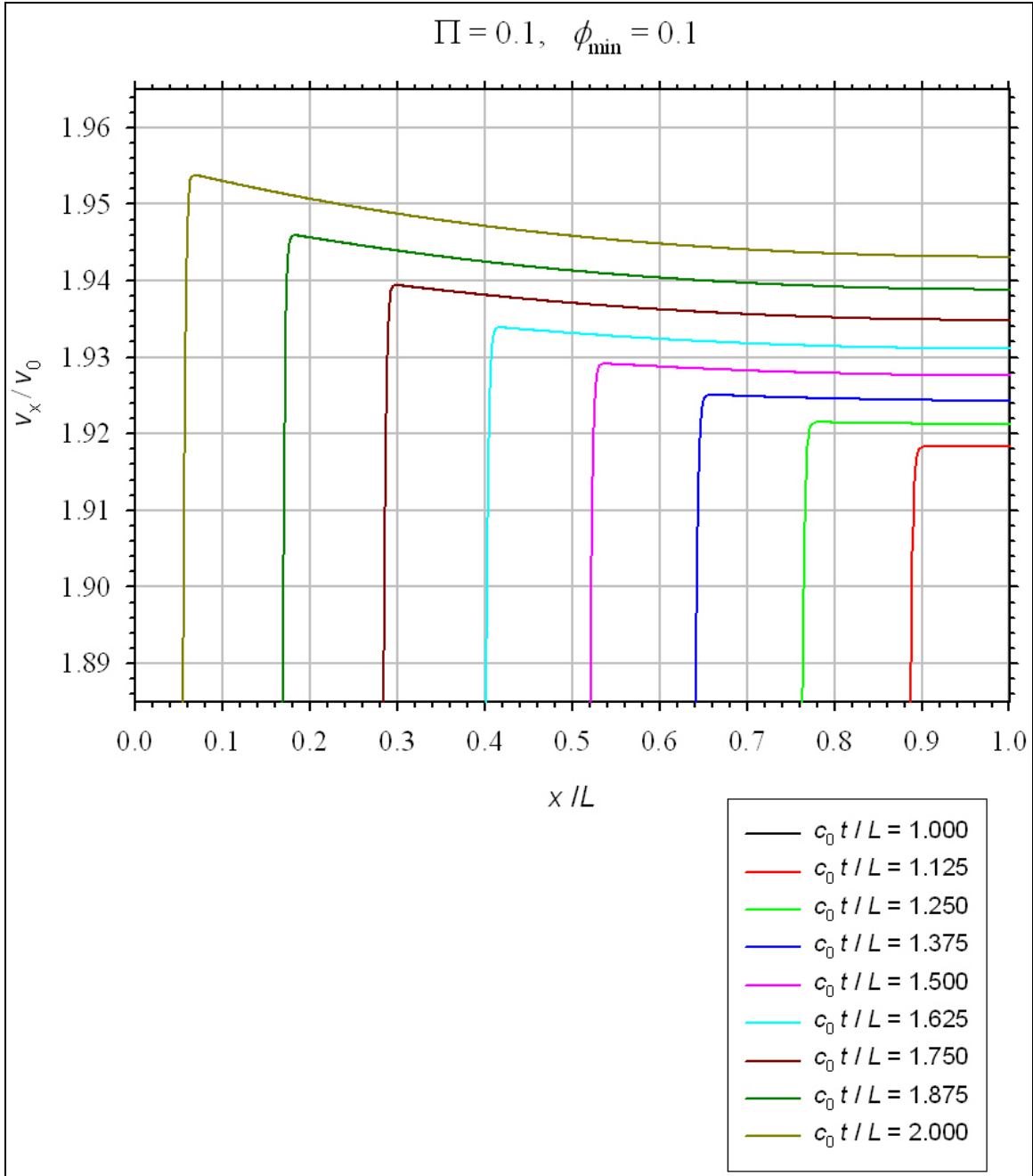


Figure A-9. Enlargement of \hat{v}_x as functions of \hat{x} for various $\hat{t} \in [1,2]$ and for $\Pi = 0.1$. ($\phi_{\min} = 0.1$.)

INTENTIONALLY LEFT BLANK

Appendix B. LS-DYNA Results for $\Pi = 0.3$

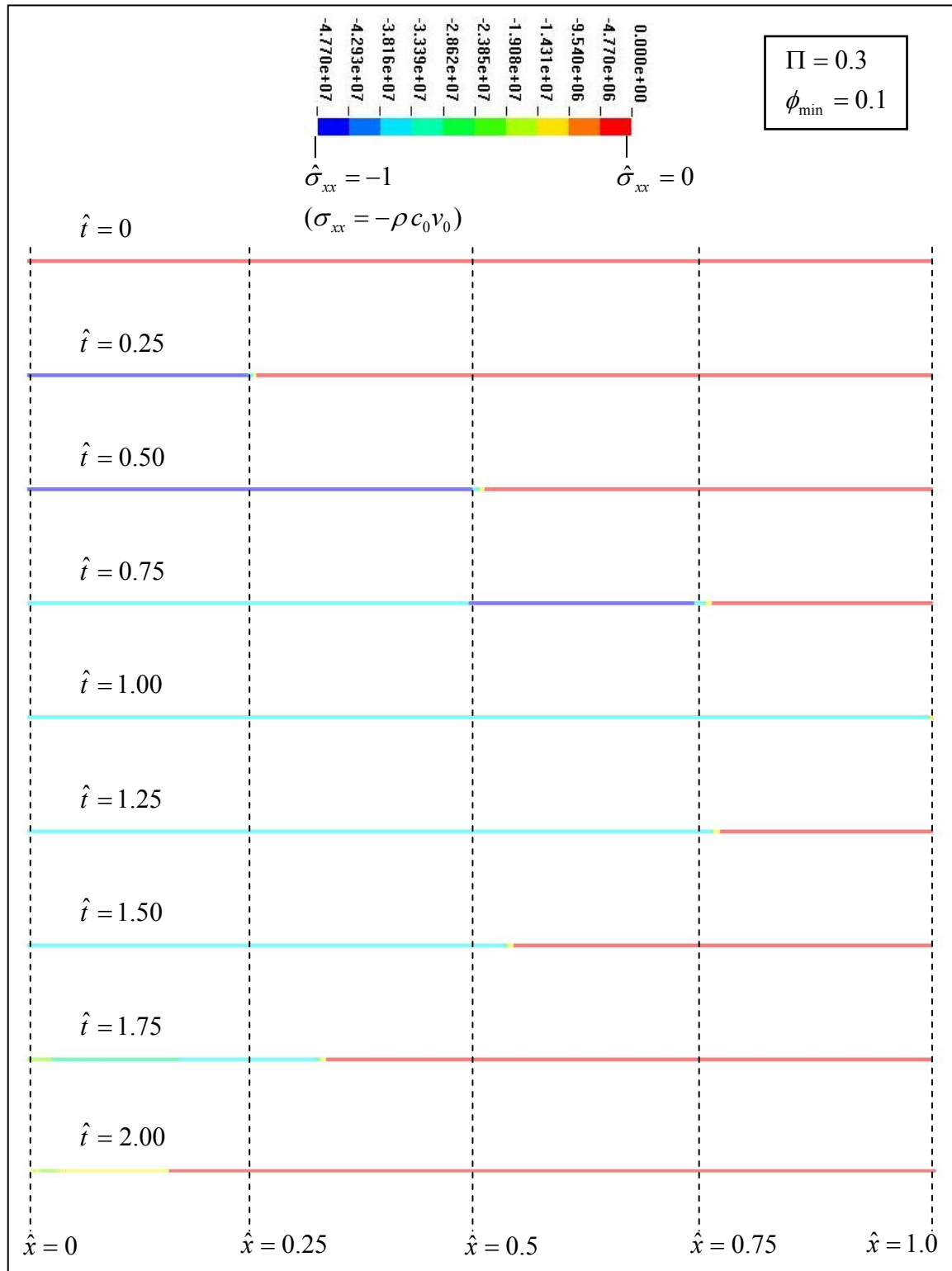


Figure B-1. Contours of $\hat{\sigma}_{xx}$ across the target plate for $\Pi = 0.3$ and $\phi_{\min} = 0.1$.

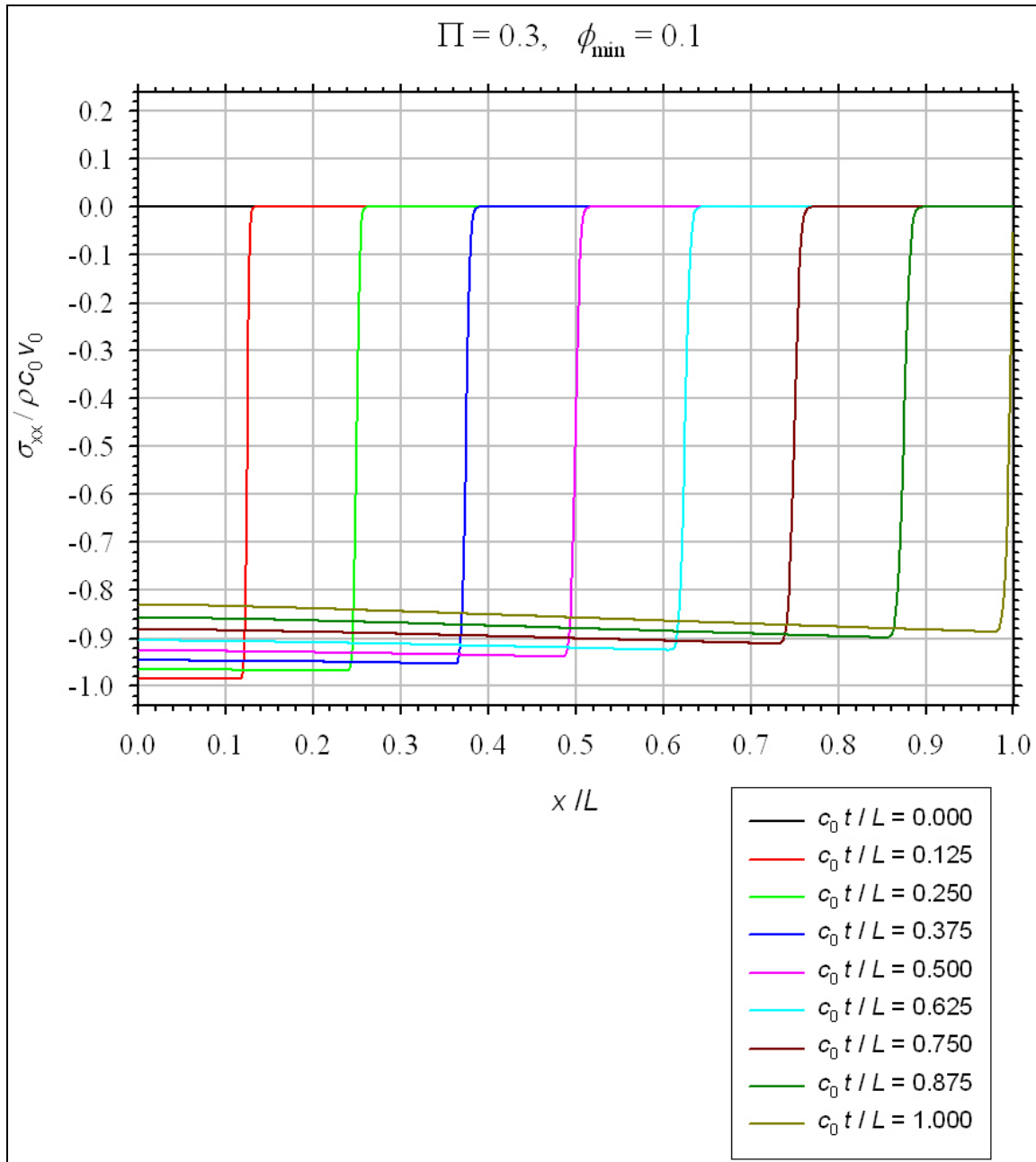


Figure B-2. $\hat{\sigma}_{xx}$ as functions of \hat{x} for various $\hat{t} \in [0,1]$ and for $\Pi = 0.3$. ($\phi_{\min} = 0.1$.)

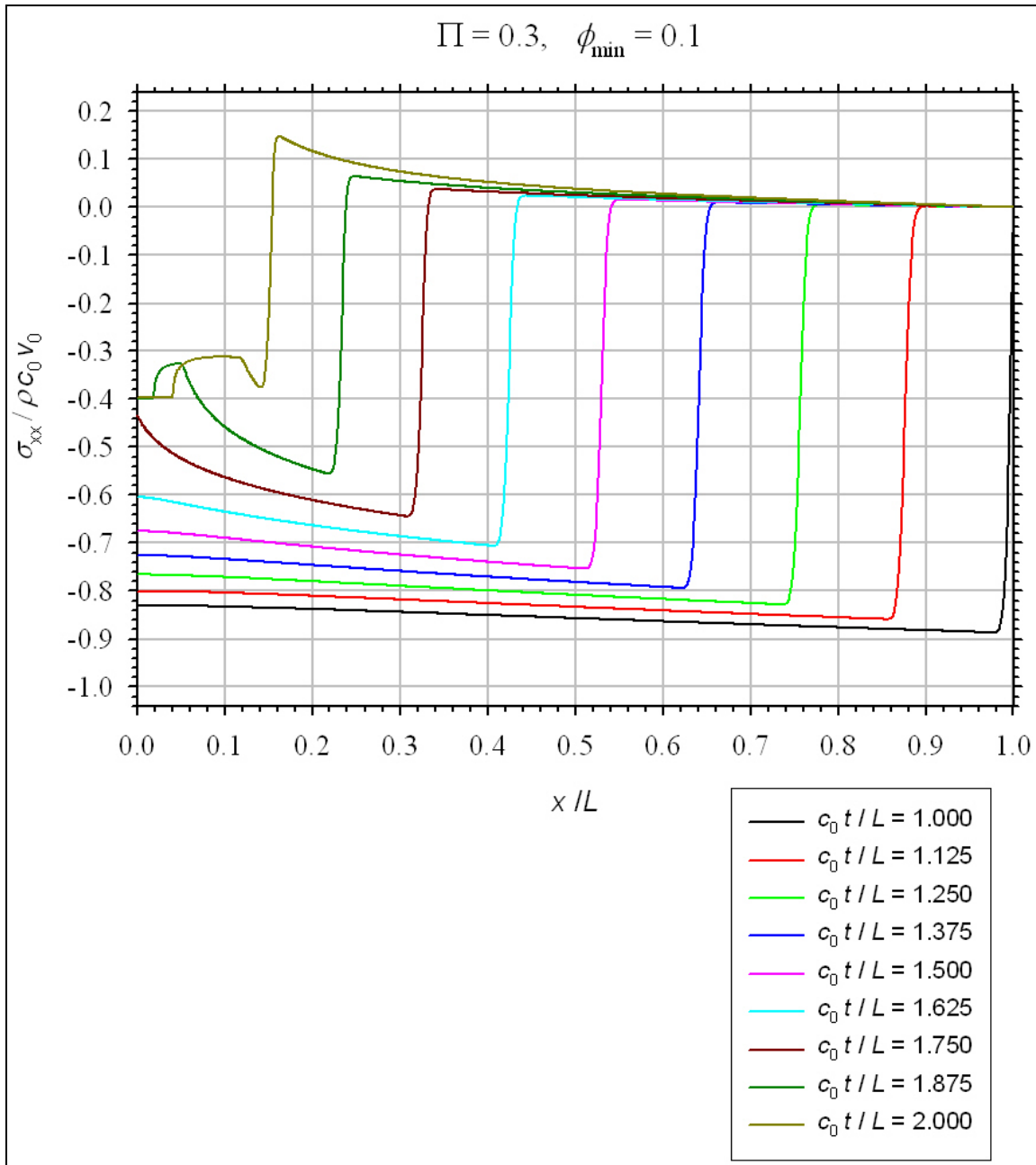


Figure B-3. $\hat{\sigma}_{xx}$ as functions of \hat{x} for various $\hat{t} \in [1,2]$ and for $\Pi = 0.3$. ($\phi_{\min} = 0.1$.)

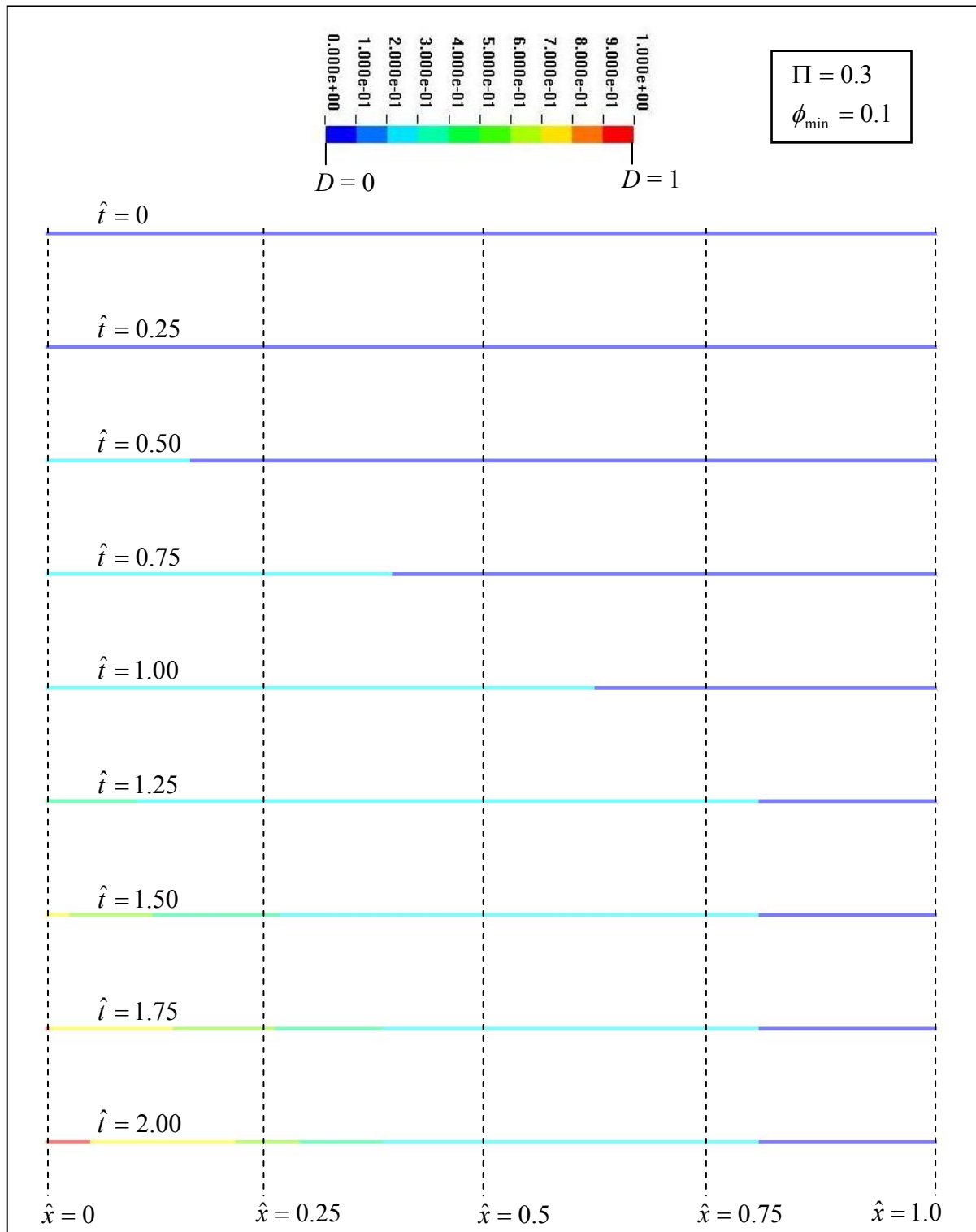


Figure B-4. Contours of D across the target plate for $\Pi = 0.3$ and $\phi_{\min} = 0.1$.

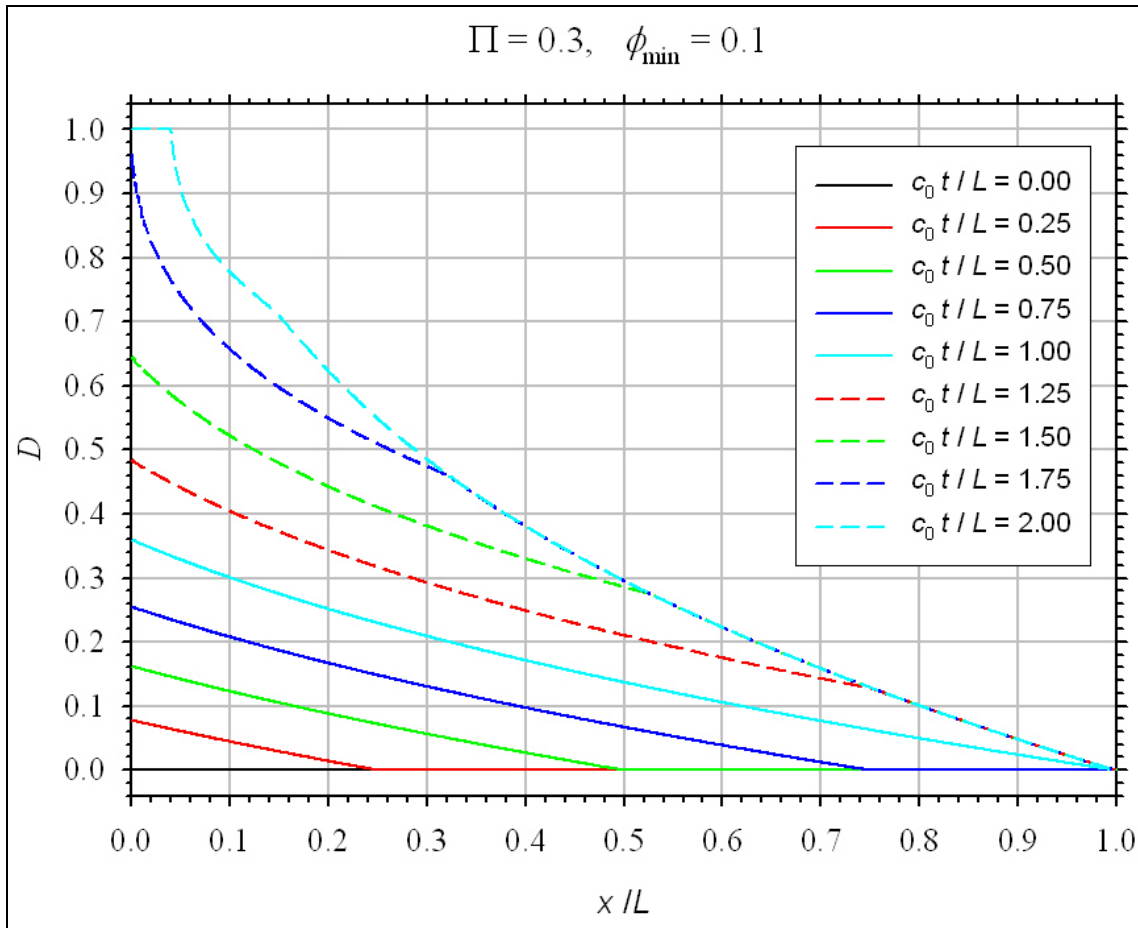


Figure B-5. D as functions of \hat{x} for various \hat{t} and for $\Pi = 0.3$. ($\phi_{\min} = 0.1$.)

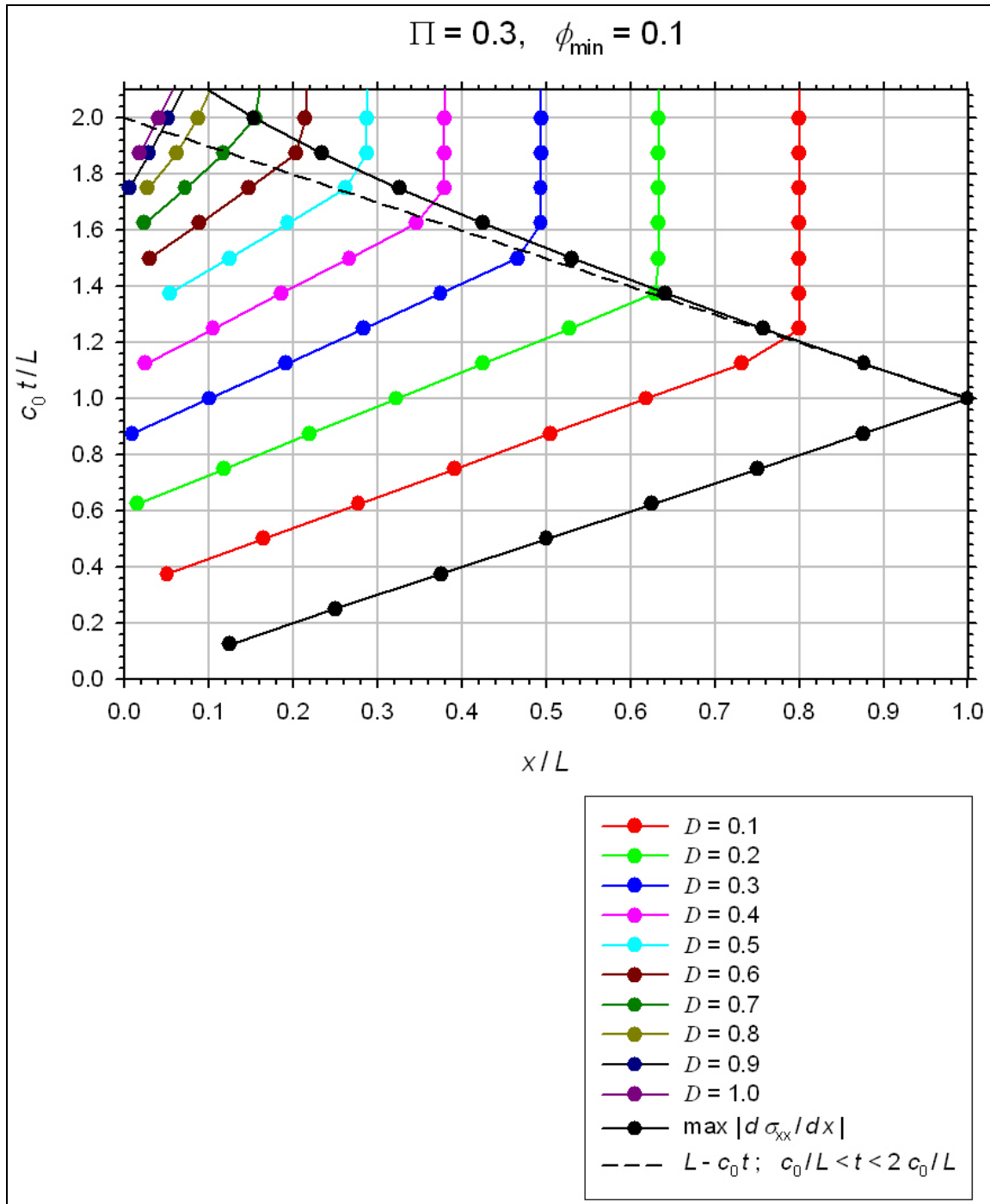


Figure B-6. D Contours in $\hat{x} - \hat{t}$ space for $\Pi = 0.3$. ($\phi_{\min} = 0.1$.)

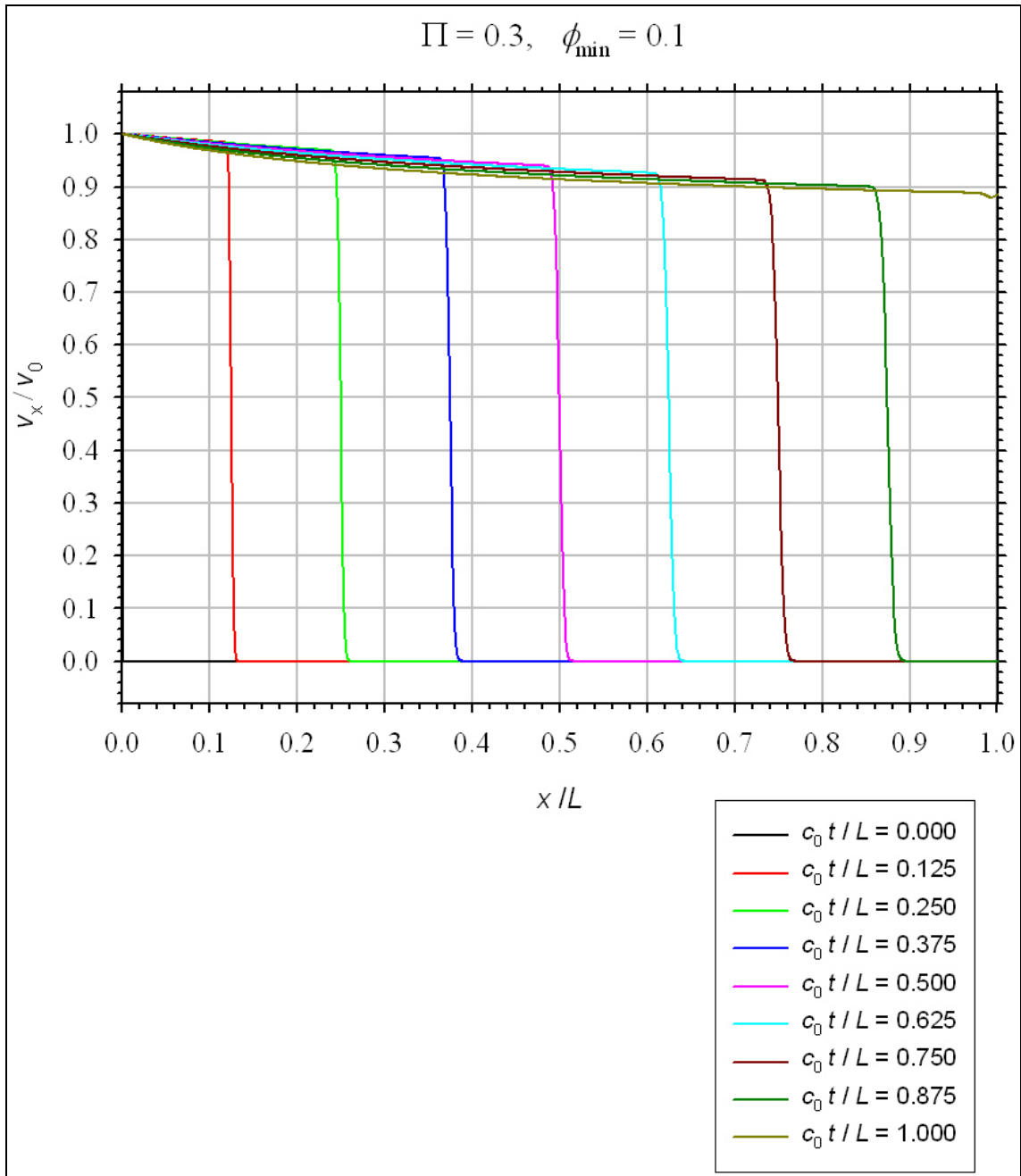


Figure B-7. \hat{v}_x as functions of \hat{x} for various $\hat{t} \in [0,1]$ and for $\Pi = 0.3$. ($\phi_{\min} = 0.1$.)

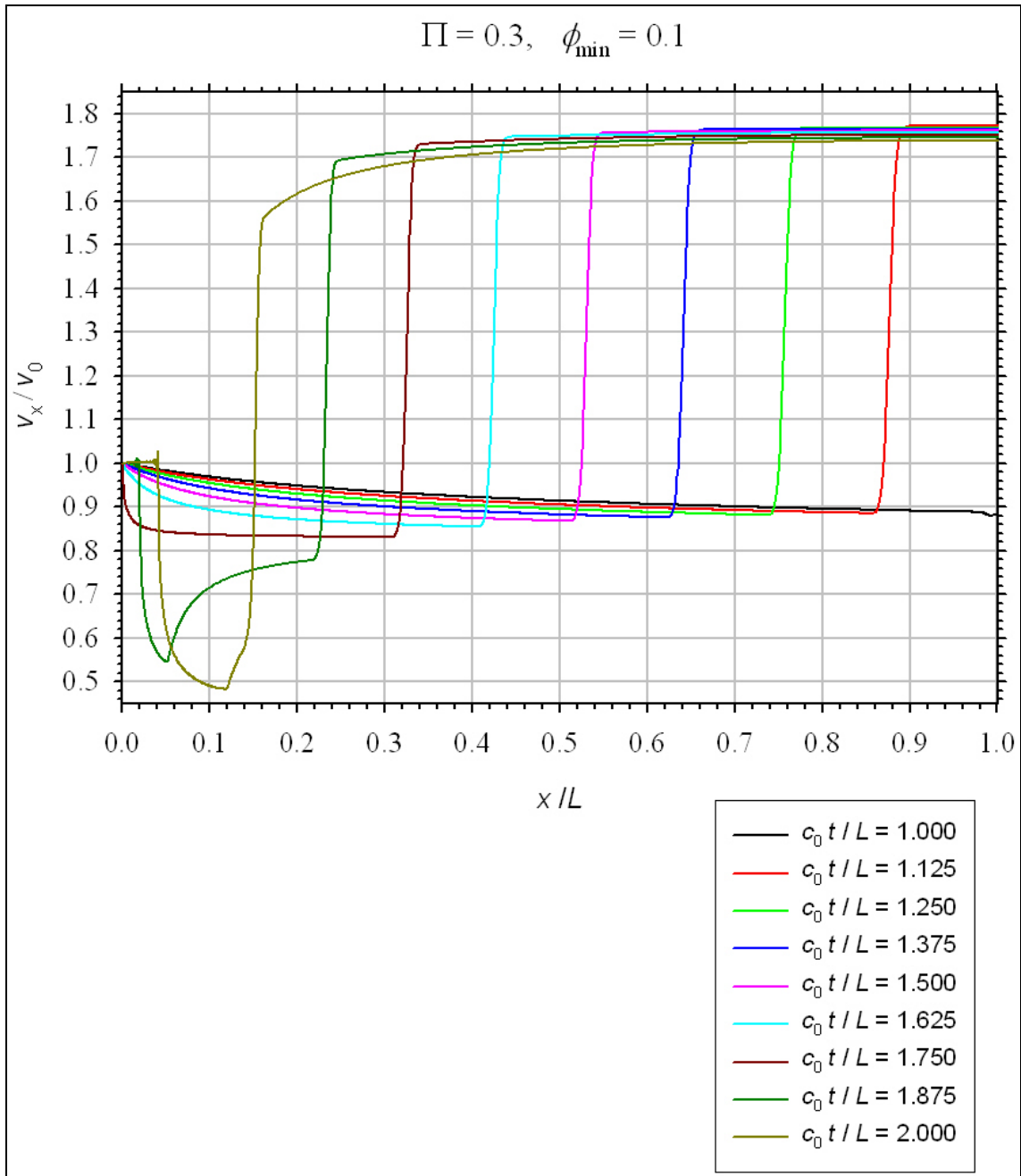


Figure B-8. \hat{v}_x as functions of \hat{x} for various $\hat{t} \in [1,2]$ and for $\Pi = 0.3$. ($\phi_{\min} = 0.1$.)

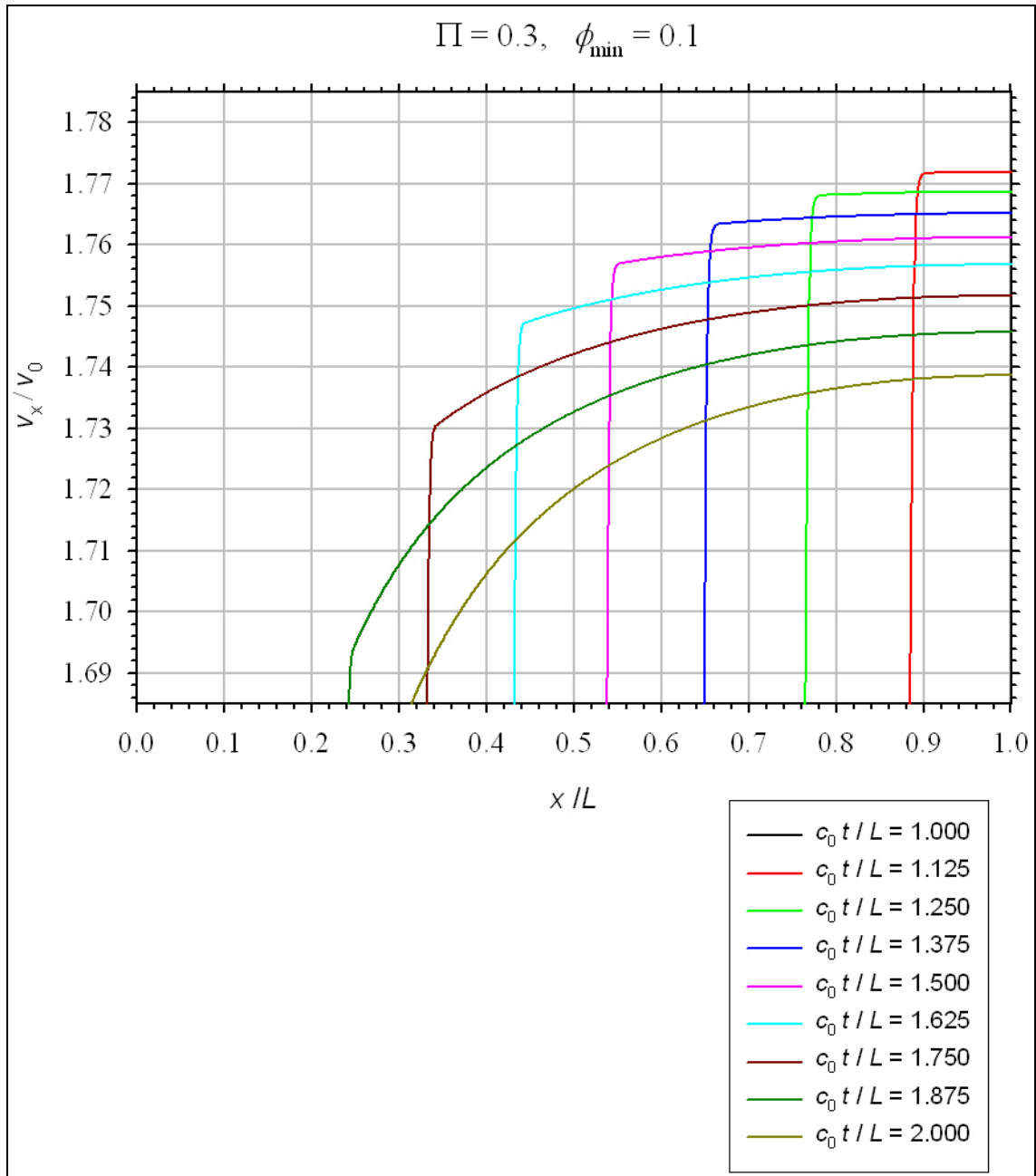


Figure B-9. Enlargement of \hat{v}_x as functions of \hat{x} for various $\hat{t} \in [1,2]$ and for $\Pi = 0.3$. ($\phi_{\min} = 0.1$.)

INTENTIONALLY LEFT BLANK

Appendix C. LS-DYNA Results for $\Pi = 0.126$

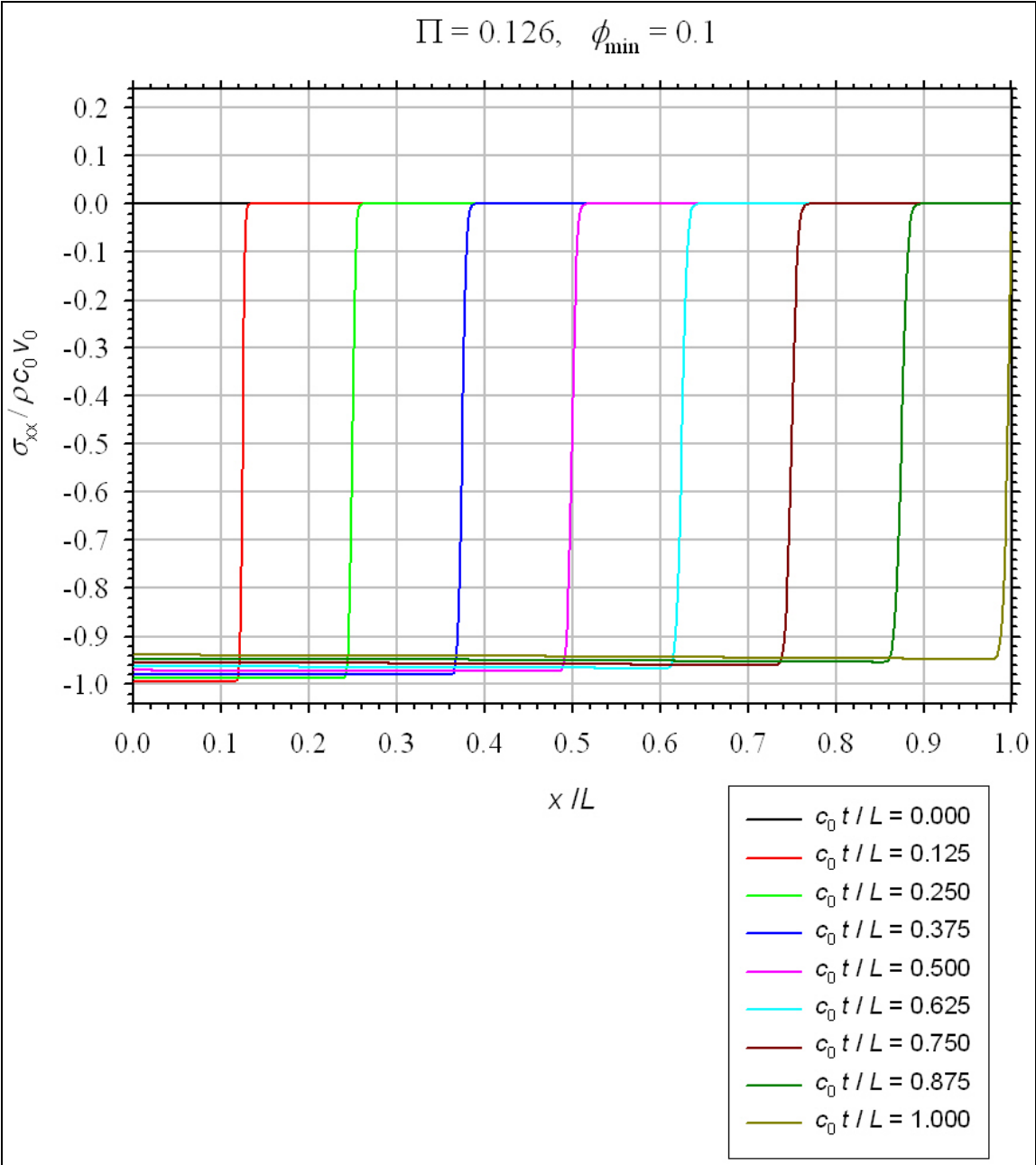


Figure C-1. $\hat{\sigma}_{xx}$ as functions of \hat{x} for various $\hat{t} \in [0,1]$ and for $\Pi = 0.126$. ($\phi_{\min} = 0.1$.)

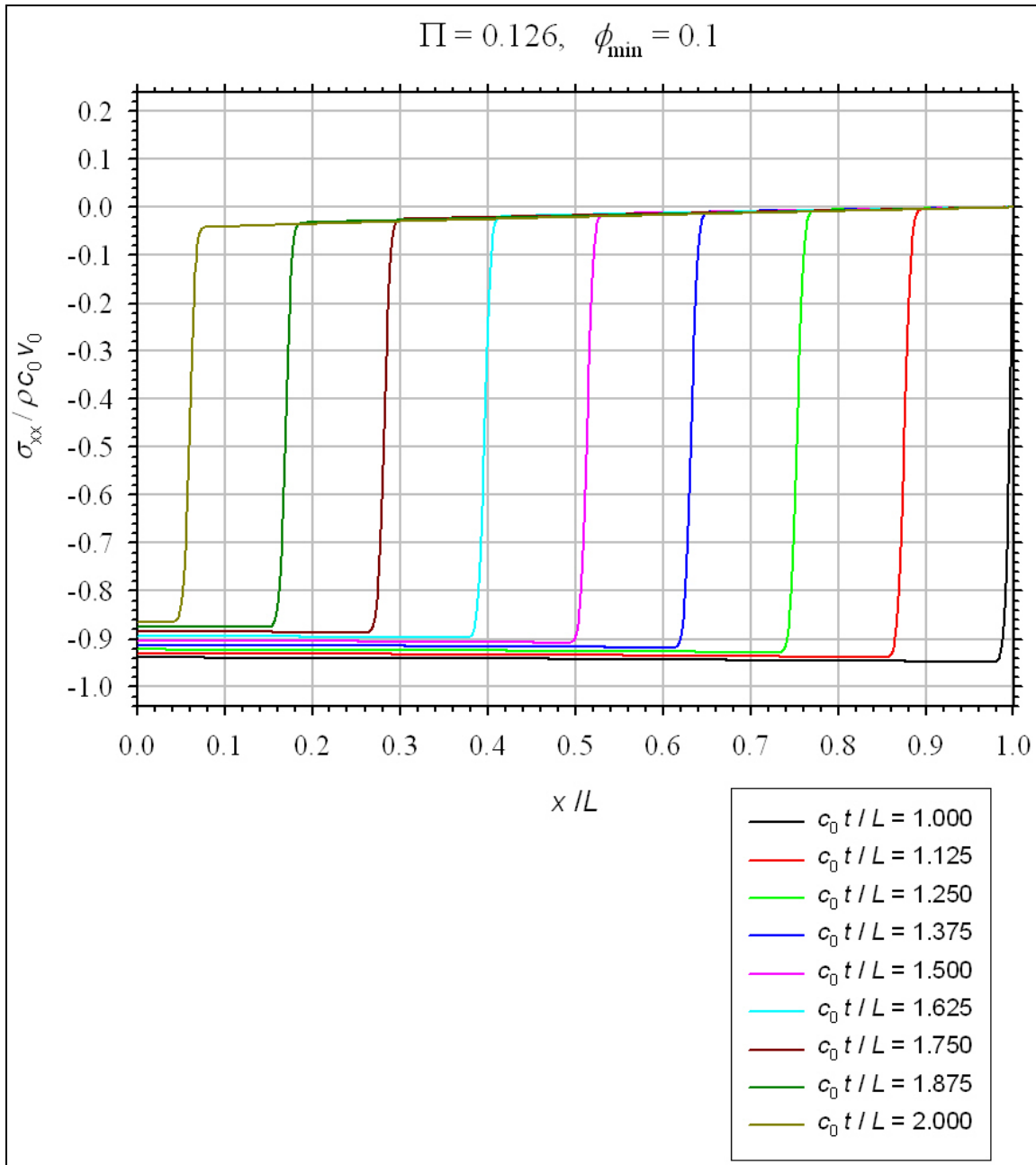


Figure C-2. $\hat{\sigma}_{xx}$ as functions of \hat{x} for various $\hat{t} \in [1,2]$ and for $\Pi = 0.126$. ($\phi_{\min} = 0.1$.)

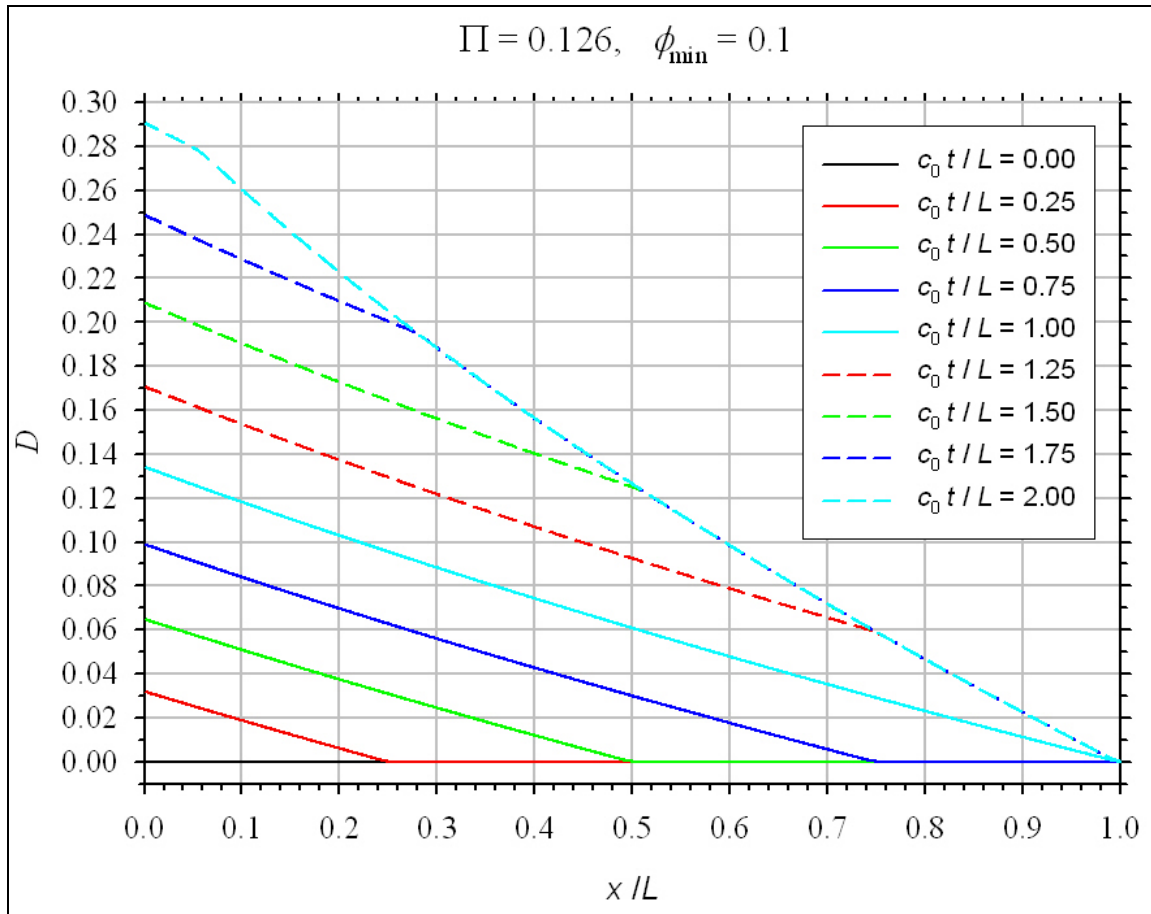


Figure C-3. D as functions of \hat{x} for various \hat{t} and for $\Pi = 0.126$. ($\phi_{\min} = 0.1$.)

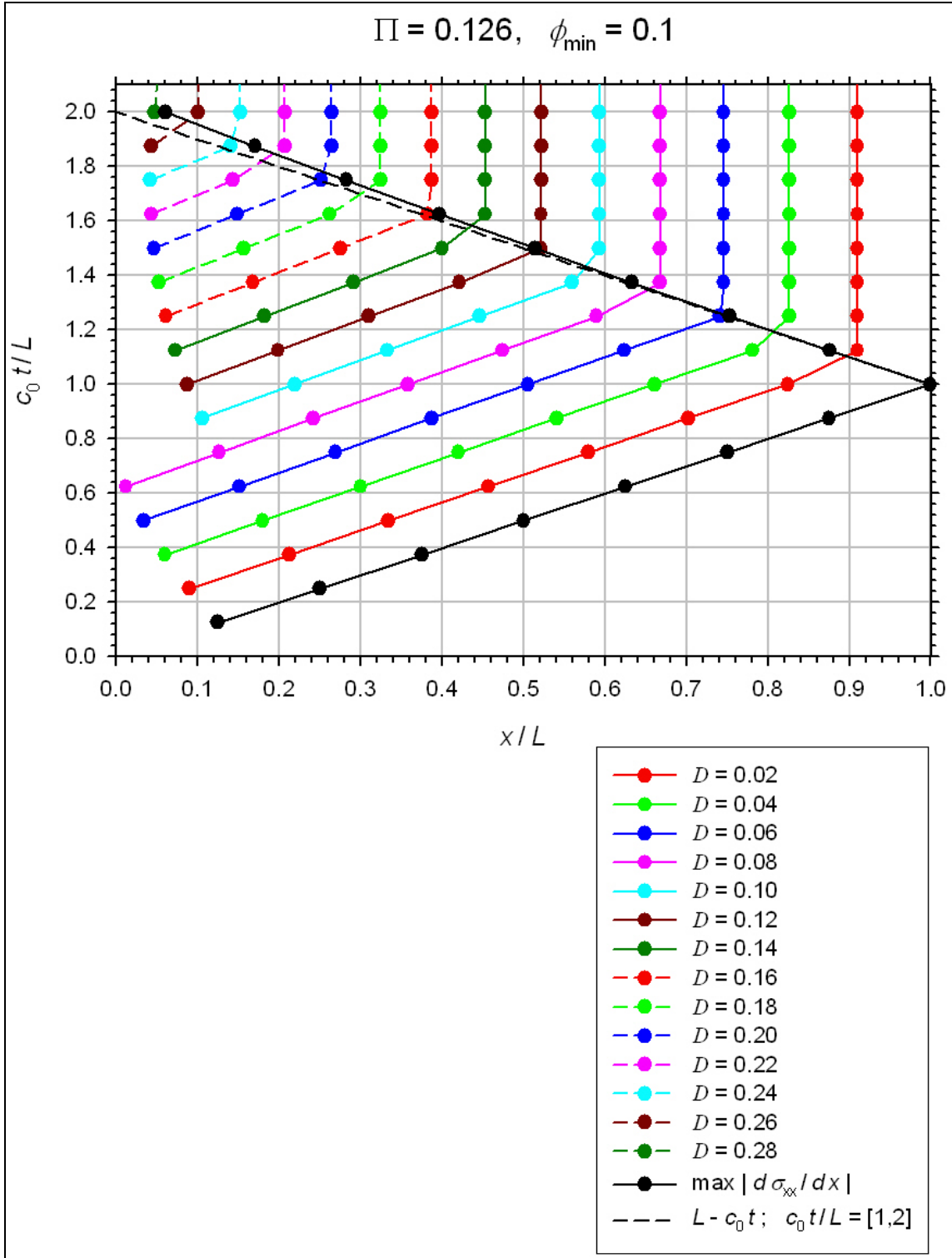


Figure C-4. D contours in $\hat{x} - \hat{t}$ space for $\Pi = 0.126$. ($\phi_{\min} = 0.1$.)

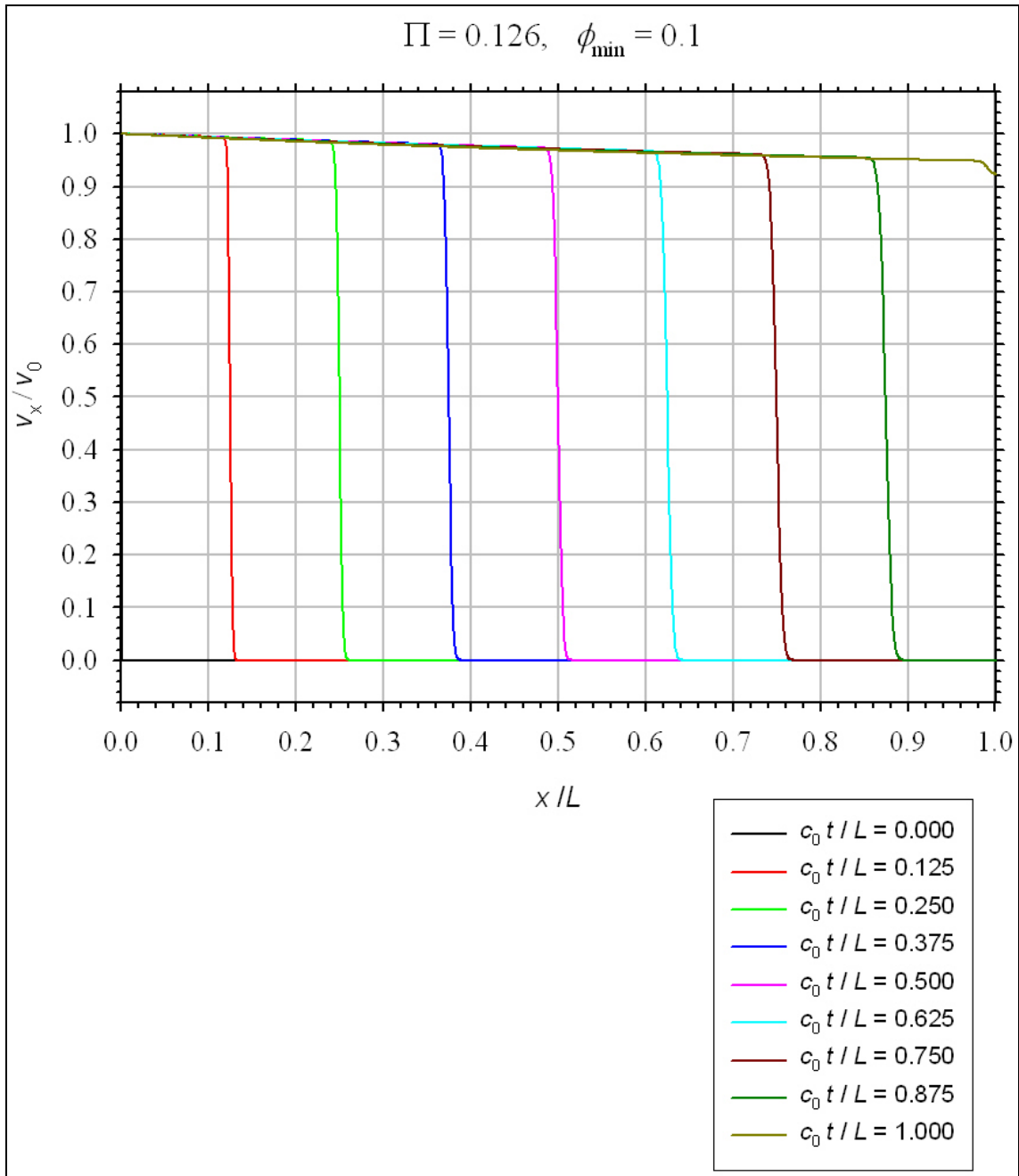


Figure C-5. \hat{v}_x as functions of \hat{x} for various $\hat{t} \in [0,1]$ and for $\Pi = 0.126$. ($\phi_{\min} = 0.1$.)

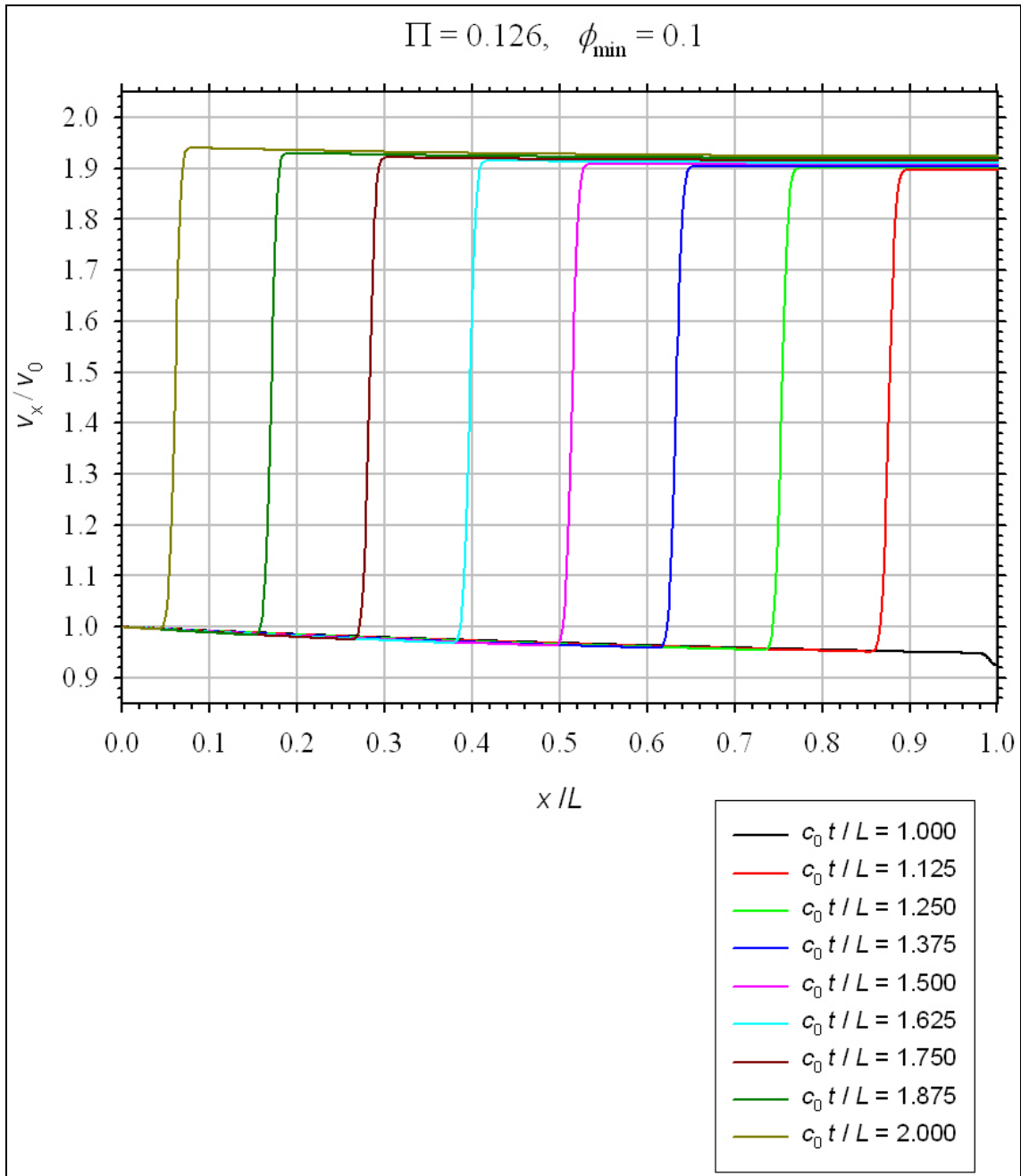


Figure C-6. \hat{v}_x as functions of \hat{x} for various $\hat{t} \in [1,2]$ and for $\Pi = 0.126$. ($\phi_{\min} = 0.1$.)

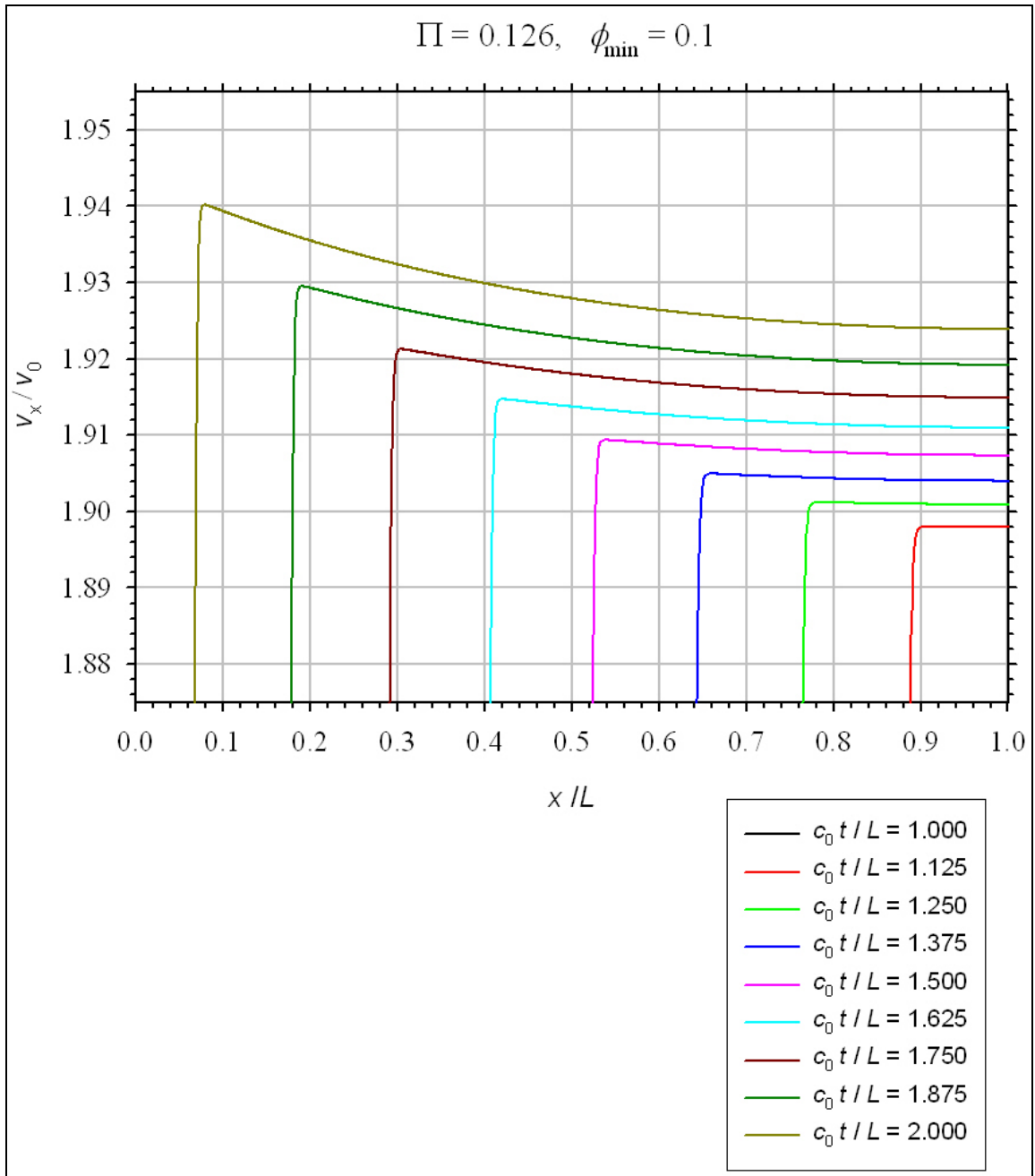


Figure C-7. Enlargement of \hat{v}_x as functions of \hat{x} for various $\hat{t} \in [1,2]$ and for $\Pi = 0.126$. ($\phi_{\min} = 0.1$.)

List of Symbols

C	material constant introduced by the damage model
D	damage measure
D_1	$O(\Pi)$ term of the D expansion
\mathbf{E}	Green (Lagrangian) strain tensor
E_{XX}, E_{YY}, E_{ZZ}	normal components of the Green strain tensor
E_{XY}, E_{YZ}, E_{ZX}	shear components of the Green strain tensor
\mathbf{F}	deformation gradient tensor
\mathbf{I}	identity tensor
L	target plate thickness
L_0	initial edge length of the initially cubic 8-node brick element
\mathbf{S}	second Piola-Kirchhoff stress tensor
S_{XX}, S_{YY}, S_{ZZ}	normal components of the Piola-Kirchhoff stress
S_{XY}, S_{YZ}, S_{ZX}	shear components of the Piola-Kirchhoff stress
W_0	elastic strain energy per unit volume
\mathbf{X}	position vector in the reference system
X, Y, Z	material coordinates
a_x, b_x, \dots, g_z	functions of time appearing in an element's shape function
c_0	longitudinal wave speed of undamaged material
\mathbf{e}	infinitesimal strain tensor
e_{xx}, e_{yy}, e_{zz}	normal components of the infinitesimal strain tensor
e_{xy}, e_{yz}, e_{zx}	shear components of the infinitesimal strain tensor
t	time
\mathbf{u}	displacement vector
u_x, u_y, u_z	components of displacement
u_0	u_x solution for no damage
u_1	$O(\Pi)$ term of the u_x expansion
\mathbf{v}	velocity vector
\mathbf{u}	displacement vector
v_0	velocity of the target's impacted face
v_x, v_y, v_z	components of velocity
\mathbf{x}	position vector in the "laboratory" system
x, y, z	spatial coordinates
δ_{ij}	Kronecker delta tensor
ϕ	degradation function of D
ϕ_{\min}	material constant introduced by the damage model

μ	shear modulus of elasticity
ν	Poisson's ratio
Π	dimensionless group
ψ	Helmholtz free energy per volume
ρ	current density
σ	Cauchy stress tensor
$\sigma_{xx}, \sigma_{yy}, \sigma_{zz}$	normal components of Cauchy stress
$\sigma_{xy}, \sigma_{yz}, \sigma_{zx}$	shear components of Cauchy stress

NO. OF
COPIES ORGANIZATION

1 DEFENSE TECHNICAL
(PDF INFORMATION CTR
ONLY) DTIC OCA
8725 JOHN J KINGMAN RD
STE 0944
FORT BELVOIR VA 22060-6218

1 US ARMY RSRCH DEV & ENGRG CMD
SYSTEMS OF SYSTEMS
INTEGRATION
AMSRD SS T
6000 6TH ST STE 100
FORT BELVOIR VA 22060-5608

2 INST FOR ADVNCD TCHNLGY
THE UNIV OF TEXAS AT AUSTIN
ATTN S BLESS S SATAPATHY
3925 W BRAKER LN STE 400
AUSTIN TX 78759-5316

1 DIRECTOR
US ARMY RESEARCH LAB
IMNE ALC IMS
2800 POWDER MILL RD
ADELPHI MD 20783-1197

1 DIRECTOR
US ARMY RESEARCH LAB
AMSRD ARL CI OK TL
2800 POWDER MILL RD
ADELPHI MD 20783-1197

2 DIRECTOR
US ARMY RESEARCH LAB
AMSRD ARL CS OK T
2800 POWDER MILL RD
ADELPHI MD 20783-1197

4 DIR ARO
ATTN A RAJENDRAN A CROWSON
B LAMATTINA TECH LIB
PO BOX 12211
RTP NC 27709-2211

2 ARMY HIGH PERFORMANCE
COMPUTING CTR
ATTN T HOLMQUIST S BEISSEL
1200 WASHINGTON AVE SOUTH
MINNEAPOLIS MN 55415

1 UNIV OF ALABAMA
ENGINEERING MECHANICS
ATTN S E JONES
PO BOX 870278
TUSCALOOSA AL 34587-0278

NO. OF
COPIES ORGANIZATION

2 NORTHWESTERN UNIV
MECHANICAL ENGINEERING
ATTN W K LIU H ESPINOSA
EVANSTON IL 60208

1 NORTHWESTERN UNIV
CIVIL ENGINEERING
ATTN T BELYTSCHKO
EVANSTON IL 60208

1 UNIV OF MISSOURI ROLLA
CIVIL ENGINEERING DEPT
ATTN W SCHONBERG
ROLLA MO 65409-0030

3 JHU MECH ENG
ATTN K T RAMESH K HEMKER F ZHOU
LATROBE HALL
3400 N CHARLES ST
BALTIMORE MD 21218

1 SRI INTERNATL
ATTN D SHOCKEY
333 RAVENSWOOD AVE
MENLO PARK CA 94025-3493

1 NORTH CAROLINA STATE UNIV
DEPT MECH AND AEROSPACE ENG
ATTN M ZIKRY
BOX 7910
RALEIGH NC 27695-7910

1 UNIV OF CINCINNATI
COLLEGE OF ENGINEERING
ATTN A TABIEI
787 RHODES HALL
PO BOX 210070
CINCINNATI OH 45221-0070

2 PURDUE UNIV
AEROSPACE ENGINEERING
ATTN W CHEN C T SUN
315 N GRANT ST
WEST LAFAYETTE IN 47907-2023

1 CALIFORNIA INST OF TECH
AERONAUTICS AND APPLIED MECHANICS
ATTN M ORTIZ
PASADENA CA 91125

1 DYNA EAST CORP
ATTN W FLIS
3620 HORIZON DRIVE
KING OF PRUSSIA PA 19406-2647

NO. OF
COPIES ORGANIZATION

2 SOUTHWEST RSCH INST
ENGR AND MAT SCI DIV
ATTN C ANDERSON J WALKER
6220 CULEBRA ROAD
PO DRAWER 28510
SAN ANTONIO TX 78228-0510

1 UNIV OF DAYTON RSRCH INST
ATTN N S BRAR
300 COLLEGE PARK
DAYTON OH 45469-0182

1 VIRGINIA TECH
ENGINEERING SCI & MECH
ATTN R BATRA
220 NORRIS HALL
BLACKSBURG VA 24061

1 LIVERMORE SOFTWARE TECH CORP
ATTN J HALLQUIST
2876 WAVERLY WAY
LIVERMORE CA 94550-1740

1 APPLIED RSCH ASSOCIATES
ATTN D E GRADY
4300 SAN MATEO BLVD NE
SUITE A 220
ALBUQUERQUE NM 87110

5 DIR SANDIA NATL LABS
ATTN M KIPP E HERTEL T VOGLER
R BRANNON TECH LIB
PO BOX 5800
ALBUQUERQUE NM 87185-5800

1 US ARMY TACOM ARDEC
ATTN AMSTA AR WEE C E BAKER
PICATINNY ARSENAL NJ 07806-5000

3 DIR LANL
ATTN D MANDEL G GRAY
TECH LIB
PO BOX 1663
LOS ALAMOS NM 87545

1 INTERNATL RSCH ASSOCIATES
ATTN D ORPHAL
4450 BLACK AVE STE E
PLEASANTON CA 94566-6145

NO. OF
COPIES ORGANIZATION

ABERDEEN PROVING GROUND

1 DIRECTOR
US ARMY RSCH LAB
ATTN AMSRD ARL CI OK TECH LIB
BLDG 4600

2 DIRECTOR
US ARMY RSCH LAB
ATTN AMSRD ARL CI HC A MARK
R NAMBURU
BLDG 394

1 DIRECTOR
US ARMY RSCH LAB
ATTN AMSRD ARL SL BB D BELY
BLDG 328

1 DIRECTOR
US ARMY RSCH LAB
ATTN AMSRD ARL SL BE R SAUCIER
BLDG 328

5 DIRECTOR
US ARMY RSCH LAB
ATTN AMSRD ARL WM J SMITH D LYON
M FERREN-COKER J MCCAULEY
T WRIGHT
BLDG 4600

1 DIRECTOR
US ARMY RSCH LAB
ATTN AMSRD ARL WM B R COATES
BLDG 309

1 DIRECTOR
US ARMY RSCH LAB
ATTN AMSRD ARL WM BF S WILKERSON
BLDG 390

1 DIRECTOR
US ARMY RSCH LAB
ATTN AMSRD ARL WM M S MCKNIGHT
BLDG 4600

9 DIRECTOR
US ARMY RSCH LAB
ATTN AMSRD ARL WM MB R DOWDING
D HOPKINS W DEROSSET
B POWERS M MINNICINO
J SOUTH J TZENG
A FRYDMAN M STAKER
BLDG 4600

NO. OF
COPIES ORGANIZATION

- 3 DIRECTOR
US ARMY RSCH LAB
ATTN AMSRD ARL WM MB M BERMAN
M CHOWDHURY T H LI
BLDG 203
- 9 DIRECTOR
US ARMY RSCH LAB
ATTN AMSRD ARL WM MD W ROY
B CHEESEMAN G GAZONAS
J LASALVIA E CHIN
C FOUNTZOULAS B SCOTT
S WOLF C F YEN
BLDG 4600
- 1 DIRECTOR
US ARMY RSCH LAB
ATTN AMSRD ARL WM T B BURNS
BLDG 309
- 3 DIRECTOR
US ARMY RSCH LAB
ATTN AMSRD ARL WM TA M BURKINS
C HOPPEL W GOOCH
BLDG 393
- 3 DIRECTOR
US ARMY RSCH LAB
ATTN AMSRD ARL WM TB P BAKER
R BITTING R SKAGGS
BLDG 309
- 28 DIRECTOR
US ARMY RSCH LAB
ATTN AMSRD ARL WM TD
T BJERKE S BILYK
M RAFTENBERG (20 CYS)
M GREENFIELD
E RAPACKI D CASEM
J CLAYTON M SCHEIDLER
K IYER
BLDG 4600
- 5 DIRECTOR
US ARMY RSCH LAB
ATTN AMSRD ARL WM TC
K KIMSEY L MAGNESS
D SCHEFFLER S SCHRAML
W WALTERS
BLDG 309
- 1 DIRECTOR
US ARMY RSCH LAB
ATTN AMSRD ARL WM TD B LOVE
BLDG 309

NO. OF
COPIES ORGANIZATION

- 1 P CHANTERET
INSTITUT SAINT-LOUIS
MULHOUSE
FRANCE
- 2 RAFAEL BALLISTICS CTR
M MAYSELESS ZVI ROSENBERG
PO BOX 2250
HAIFA 31021
ISRAEL
- 1 UNIV OF WATERLOO
MECHANICAL ENGNRG
M J WORSWICK
200 UNIVERSITY AVE
WEST WATERLOO
ONTARIO N2L3G1
CANADA
- 1 ARL ERO
S SAMPATH
AERO MECH ENG
223 MARYLEBONE RD
LONDON NW1 5TH
UNITED KINGDOM
- 1 AMC SCI & TECH CTR
EUROPE
T J MULKERN
POSTFACH 81
55247 MAINZ KASTEL
GERMANY
- 2 FRAUNHOFER-INSTITUT
ERNST-MACH-INSTITUT
V HOHLER E STRASSBURGER
ECKERSTRASSE 4
79104 FREIBURG
GERMANY